

NASA Contractor Report 4022

Application of Satellite Data to the Variational Analysis of the Three Dimensional Wind Field

Barbara Ann Chance

CONTRACT NAS8-35530
OCTOBER 1986



NASA Contractor Report 4022

Application of Satellite Data to the Variational Analysis of the Three Dimensional Wind Field

Barbara Ann Chance
University of Illinois
Urbana-Champaign, Illinois

Prepared for
George C. Marshall Space Flight Center
under Contract NAS8-35530

NASA
National Aeronautics
and Space Administration
**Scientific and Technical
Information Branch**

1986

ACKNOWLEDGEMENTS

I would like to thank my parents, Richard and Mary Chance. Without their support and encouragement this effort would not have been possible.

Special thanks to my research advisors, Drs. Gary Achtemeier and Stanley Kidder. They showed never ending patience throughout this work, and shared with me their stimulating knowledge. Thanks also to Dr. John Gyakum, who served as my academic advisor, for providing his guidance.

I am indebted to Ms. Donna Isard and Mr. Robert Scott for their assistance in acquiring the necessary data, and also to Dr. Harry Ochs for generously allowing me to use his computing equipment.

This effort was supported by NASA/Marshall Space Flight Center and the Universities Space Research Association under contract NAS8-35530.

PRECEDING PAGE BLANK NOT FILMED

TABLE OF CONTENTS

Chapter	Page
I. INTRODUCTION	1
II. DESCRIPTION OF METHODS	4
A. Kinematic Method	4
B. Adiabatic Method	6
C. Variational Method	9
1. Determination of Weights	13
III. DATA AND SYNOPTIC AND MESOSCALE CONDITIONS	19
IV. RESULTS	24
A. Vertical Velocity Results: Horizontal Fields	24
B. Vertical Velocity Results: Vertical Profiles	51
V. DISCUSSION	64
APPENDIX A	67
APPENDIX B	79
LIST OF REFERENCES	82

PRECEDING PAGE BLANK NOT FILMED

LIST OF TABLES

Table	Page
2.1. Root mean square error (RMSE) of observed horizontal velocities.	14
3.1. Number of rawinsonde stations reporting during AVE-SESAME I.	19
A.1. Non-dimensionalized constants for analytic stream function.	69
B.1. Root mean square error (RMSE) of observed temperatures.	81

LIST OF FIGURES

Figure	Page
2.1. Vertical velocity fields (cm/s) at 550 mb calculated with adiabatic method. Temperature tendencies are estimated by a) 6-hour centered difference and by b) Panofsky's approximation.	8
2.2. Schematic of sigma-pressure coordinate system.	10
3.1. Domain for data set of AVE-SESAME I. Bullseyes denote locations of observations, x's denote locations of vertical velocity profiles, and dashed lines enclose data-rich region.	20
3.2. Schematic of variable locations upon grid.	22
4.1. Vertical velocity fields (cm/s) for 12Z 10 April 1979 calculated by the O'Brien adjusted kinematic method at a) 150 mb and b) 450 mb.	25
4.2. Vertical velocity fields (cm/s) for 12Z 10 April 1979 calculated by the adiabatic method at a) 150 mb and b) 450 mb.	26
4.3. Field of $\log(\pi_2)$ for 12Z 10 April 1979 at 450 mb.	28
4.4. Fields of a) static stability parameter (K/layer) and b) clouds with relative humidity for 12Z 10 April 1979 at 450 mb.	29
4.5. GOES infrared image for 1230Z 10 April 1979.	30
4.6. Vertical velocity fields (cm/s) for 12Z 10 April 1979 calculated by the variational algorithm at a) 150 mb and b) 450 mb. In b), bold lines indicate precipitation echoes taken from radar summary and dashed line is $\pi_2 = 10^0$ contour.	32
4.7. Vertical velocity fields (cm/s) for 18Z 10 April 1979 calculated by the O'Brien adjusted kinematic method at a) 150 mb and b) 450 mb.	34
4.8. Vertical velocity fields (cm/s) for 18Z 10 April 1979 calculated by the adiabatic method at a) 150 mb and b) 450 mb.	35
4.9. Field of $\log(\pi_2)$ for 18Z 10 April 1979 at 450 mb.	36
4.10. Fields of a) static stability parameter (K/layer) and b) clouds with relative humidity for 18Z 10 April 1979 at 450 mb.	37

4.11.	GOES infrared image for 1800Z 10 April 1979.	38
4.12.	Vertical velocity fields (cm/s) for 18Z 10 April 1979 calculated by the variational algorithm at a) 150 mb and b) 450 mb. In b), bold lines indicate precipitation echoes taken from radar summary and dashed line is $\pi_2 = 10^0$ contour.	40
4.13.	Vertical velocity fields (cm/s) for 0Z 11 April 1979 calculated by the O'Brien adjusted kinematic method at a) 150 mb and b) 450 mb.	42
4.14.	Vertical velocity fields (cm/s) for 0Z 11 April 1979 calculated by the adiabatic method at a) 150 mb and b) 450 mb.	43
4.15.	Field of $\log(\pi_2)$ for 0Z 11 April 1979 at 450 mb.	44
4.16.	Fields of a) static stability parameter (K/layer) and b) clouds with relative humidity for 0Z 11 April 1979 at 450 mb.	45
4.17.	GOES infrared image for 0000Z 11 April 1979.	46
4.18.	Vertical velocity fields (cm/s) for 0Z 11 April 1979 calculated by the variational algorithm at a) 150 mb and b) 450 mb. In b), bold lines indicate precipitation echoes taken from radar summary and dashed line is $\pi_2 = 10^0$ contour.	48
4.19.	Vertical velocity fields (cm/s) for 6Z 11 April 1979 calculated by the O'Brien adjusted kinematic method at a) 150 mb and b) 450 mb.	49
4.20.	Vertical velocity fields (cm/s) for 6Z 11 April 1979 calculated by the adiabatic method at a) 150 mb and b) 450 mb.	50
4.21.	Field of $\log(\pi_2)$ for 6Z 11 April 1979 at 450 mb.	52
4.22.	Fields of a) static stability parameter (K/layer) and b) clouds with relative humidity for 6Z 11 April 1979 at 450 mb.	53
4.23.	GOES infrared image for 0600Z 11 April 1979.	54
4.24.	Vertical velocity fields (cm/s) for 6Z 11 April 1979 calculated by the variational algorithm at a) 150 mb and b) 450 mb. In b), bold lines indicate precipitation echoes taken from radar summary and dashed line is $\pi_2 = 10^0$ contour.	55
4.25.	Vertical profiles of a) vertical motion (cm/s) and b) $\log(\pi_2)$ at northern Kansas for 12Z 10 April 1979.	57

4.26.	Vertical profiles of a) vertical motion (cm/s) and b) $\log(\pi_2)$ at central Missouri for 12Z 10 April 1979.	58
4.27.	Vertical profiles of a) vertical motion (cm/s) and b) $\log(\pi_2)$ at western Missouri for 18Z 10 April 1979.	60
4.28.	Vertical profiles of a) vertical motion (cm/s) and b) $\log(\pi_2)$ at northern Oklahoma for 0Z 11 April 1979.	62
A.1.	Plot of non-divergent, analytic stream function (solid lines). Dashed lines are corresponding isotachs. All values are non-dimensionalized.	68
A.2.	Schematic of staggered grid used for finite difference approximation of horizontal derivatives.	70
A.3.	Results of the objectively analyzed stream function (solid lines) using a) regularly-spaced data points and b) and c) 20 randomly-spaced data point. Bullseyes indicate locations of data points and dashed lines are isotachs from objectively analyzed horizontal velocities. ...	74
A.4.	Results of objectively analyzed stream function (solid lines) using 20 non-randomly-spaced data points with a concentration of points a) in the minima and b) in the region of strong gradient. Bullseyes and dashed lines as in Fig. A.3.	75
A.5.	RMS error calculated for a) analyzed ψ fields with regularly-spaced data points (case I is 4 gsu spacing), b) analyzed ψ fields with random (cases II and III) and non-random (cases IV and V) spacings, c) vertical velocity derived from ψ fields of a), and d) vertical velocity derived from ψ fields of b).	77

CHAPTER I

INTRODUCTION

Vertical velocity is a useful atmospheric parameter because it can identify areas where significant weather such as clouds and precipitation are likely to occur. For mesoscale dynamics, the magnitude of the vertical component of the wind is about two or three orders smaller than the magnitude of the horizontal components. Since the quantity is so small, it is difficult to obtain direct measurements which are reliable. Instead, various methods have been devised to derive the vertical component of motion from other available parameters such as pressure, temperature, or horizontal winds. Some of these are described by Miller and Panofsky (1958).

Many studies have been undertaken to compare the results of various computation methods of vertical velocity for synoptic and large scales of motion (eg., Panofsky, 1946; O'Neill, 1966; Djuric, 1969; Smith, 1971; Kung, 1972; Kung, 1973; Stuart, 1974; Smith and Lin, 1978; White, 1983; Lamb and Portis, 1986). For these scales of motion, the kinematic and adiabatic methods and the quasi-geostrophic omega equation are generally employed. The first two methods are described in detail by Panofsky (1946) and by Pettersen (1956). These two methods make use of the horizontal wind field, but the kinematic method is based on the concept of mass continuity, while the adiabatic method presumes isentropic flow. The third method, the quasi-geostrophic omega equation, uses a relation between vorticity advection and thermal advection to estimate vertical velocity (Holton, 1979).

Unfortunately, few vertical velocity studies have been documented for mesoscale phenomena. Holton (1979) states that since the Rossby number approaches 1 at this scale, the quasi-geostrophic omega equation is not a valid solution to vertical velocity estimation. The kinematic method is favored for the calculation of mesoscale vertical velocities (eg., Fankhauser, 1969; Fuelberg and Lee, 1983). The only assumption is hydrostatic balance, and it requires knowledge only of the divergence of the horizontal wind. Since non-divergent approximations such as geostrophic flow produce trivial kinematic results, it is necessary, then, to use actual wind observations. These data are sparse and often inaccurate. Some sources of error in wind data are due to the measuring instruments and phenomena which are of smaller scale than the station spacing. Additional inaccuracy is introduced by interpolating the sparse, irregularly-spaced data onto a gridded field and by using finite differences to approximate derivatives (eg., Kurihara, 1961; Belt and Fuelberg, 1982; Smith and Leslie, 1984).

An alternative technique for calculating vertical motion is the adiabatic method. This method incorporates the thermodynamic properties of temperature tendency, thermal advection and static stability into the calculation. This method fails, though, when the environmental lapse rate approaches the dry adiabatic lapse rate or when diabatic processes violate the assumption of adiabatic flow.

A comparison of the two independent methods shows complementary strengths and weaknesses. Strengths of the kinematic method are that 1) it is based on the simple principle of mass continuity, and 2) only knowledge of the horizontal wind field is required. Weaknesses of the kinematic method are 1) the method is very sensitive to data errors and

data interpolation, and 2) vertical integration causes errors to accumulate. A correction scheme may be implemented to reduce the bias errors; however, this may require one or more boundary conditions to be imposed (Lateef, 1967; Fankhauser, 1969; O'Brien, 1970). Advantages of the adiabatic method are that 1) additional information about the atmosphere is incorporated into the calculation and 2) there is no need to impose boundary conditions. Disadvantages of the adiabatic method are that 1) it can only be used where the flow is nearly adiabatic, 2) it requires frequent temperature observations so that temperature tendency can be accurately estimated, and 3) it becomes unstable for nearly neutral layers where the static stability parameter approaches zero.

To combine the strengths of the methods, a hybrid vertical velocity algorithm, which is a variational mesh of the kinematic and adiabatic methods, is developed. The relative weights accorded to the schemes are determined from the error variance of the measurements, cloud top temperatures deduced from the Geostationary Operational Environmental Satellite (GOES) digital infrared data, and static stability. The kinematic method is assigned greatest weight near the surface, in deep cloudy regions, and in layers of near neutral static stability. The adiabatic method receives greatest weight in layers not influenced by diabatic heating: clear regions and levels near and above the tropopause. This algorithm is tested with the Atmospheric Variability Experiment - Severe Environmental Storms and Mesoscale Experiment (AVE-SESAME) I case period (12Z 10 April - 12Z 11 April 1979) data set.

CHAPTER II

DESCRIPTION OF METHODS

A. Kinematic Method

The kinematic method is based on the conservation of mass principle. Solving for ω , the vertical component of velocity in pressure coordinates, this becomes symbolically,

$$\int_{\omega_0}^{\omega_0 + \Delta\omega} d\omega = - \int_{p_0}^{p_0 + \Delta p} \left(\frac{\partial u}{\partial x} + \frac{\partial v}{\partial y} \right) dp \quad (2.1)$$

Here, u is the x-component of motion and v is the y-component of motion.

This method vertically integrates divergence through the domain. Since non-divergent wind approximations are inappropriate, actual wind observations must be used to determine horizontal divergence. The divergence is very sensitive to errors in the horizontal wind field. Holton (1979) relates that a 10% error in one wind component can lead to a 100% error in horizontal divergence. The divergence is also very sensitive to data interpolation and to the approximation of the horizontal derivatives. Appendix A shows that these difficulties can lead to substantial vertical velocity magnitudes in a non-divergent wind field. These errors in the horizontal divergence sum upward from the bottom of a column and can become very large at the top. To help alleviate this problem, a correction method can be utilized.

One method for correcting vertical velocities is suggested by Lateef (1967) as

$$\omega'_k = \omega_k - \frac{k}{K}(\omega_K - \omega_T) \quad (2.2)$$

where the primed value is the adjusted velocity, k is an index

designating an individual layer of constant pressure depth, K is the total number of layers of constant pressure depth, ω_K is the calculated value of vertical motion at layer K , and ω_T is an estimated value at K .

Another correction technique is the O'Brien (1970) scheme. This correction technique uses mass continuity and an estimate of vertical velocity at the top of the column as constraints. From these constraints, weighted adjustments are determined and applied to the vertically integrated divergences. The value of the weights, known as Gauss precision moduli, is determined from the relative measurement accuracy of the horizontal wind.

$$\pi_i = \frac{1}{2\epsilon_i^2} \quad (2.3)$$

Here, π_i is the Gauss precision modulus and ϵ_i^2 is the error variance of a variable, i . If ϵ_v^2 represents the error variance of the horizontal wind measurement and is considered to be independent of pressure, then O'Brien's method simplifies to that of Lateef. O'Brien (1970) stated that the error in rawinsonde wind measurements increases with height. He assumes ϵ_v^2 to be a linear function of pressure; thus, the vertical velocity correction becomes

$$\omega'_k = \omega_k - \left[\frac{k(k+1)}{K(K+1)} \right] (\omega_K - \omega_T) . \quad (2.4)$$

These approaches have the unfortunate property that they force the velocity at the top of the column to a preset value and can transfer errors from the lower troposphere into the upper troposphere and stratosphere. These errors can become unrealistically large near and above the tropopause.

Kinematic vertical velocities are calculated in a case study performed by Smith (1971). In this effort, which utilized both the Lateef and O'Brien adjustments, the O'Brien correction method produced results which better represented the observed weather conditions. Pedder (1981) states, though, that the O'Brien method is only slightly better than Lateef's. He notes that O'Brien only considers the error variance of the horizontal divergence estimate. Other errors exist due to assuming a linear variation of divergence in the sampling layers and to assuming that the divergence errors are vertically uncorrelated. Pedder suggests that the nature of the wind data, for example, be considered before an optimal adjustment scheme is chosen.

Strengths of the kinematic method are that 1) it is based on the simple principle of mass continuity, and 2) only knowledge of the horizontal wind field is required, i.e. no additional processes such as heating are involved. Weaknesses of the kinematic method are that 1) the method is very sensitive to data errors and data interpolation, and 2) vertical integration causes errors to accumulate at the top of a column.

B. Adiabatic Method

The adiabatic method of calculating vertical motion includes thermodynamic properties of the atmosphere. It is derived from the First Law of Thermodynamics with the assumption that no heat is lost or gained.

$$c_p \frac{dT}{dt} - \alpha \frac{dp}{dt} = \dot{Q} = 0 \quad (2.5)$$

In this formulation, c_p is the specific heat of dry air, α is the specific volume, and \dot{Q} is the diabatic heating rate. The total

temperature derivative is expanded and ω is substituted for Dp/Dt to yield the final form.

$$\omega = \frac{\partial T / \partial t - (-\vec{V} \cdot \nabla_p T)}{s} \quad (2.6)$$

where,
$$s = \partial T / \partial p - dT / dp \quad (2.7)$$

Here $\frac{\partial T}{\partial t}$ is the temperature tendency, $-\vec{V} \cdot \nabla_p T$ is the horizontal thermal advection, and s is the static stability parameter.

The temperature tendency is a difficult quantity to estimate since frequent temperature observations are necessary. Panofsky (1964) approximates the temperature tendency with one-half the value of the temperature advection. Fig. 2.1 shows two adiabatic vertical velocity fields. One uses three hourly temperature observations to calculate temperature tendency, and the other uses Panofsky's approximation. The vertical velocity fields are very similar. The sign of the vertical velocity is the same in most areas, but the magnitudes are somewhat different.

Advantages of the adiabatic method are that 1) additional information about the atmosphere is incorporated into the calculation and 2) there is no need to impose boundary conditions. Disadvantages of the adiabatic method are that 1) it can only be used where the flow is nearly adiabatic, 2) it is beneficial to have frequent temperature observations so that temperature tendency can be accurately estimated, and 3) it becomes unstable for nearly neutral layers where the static stability parameter approaches zero.

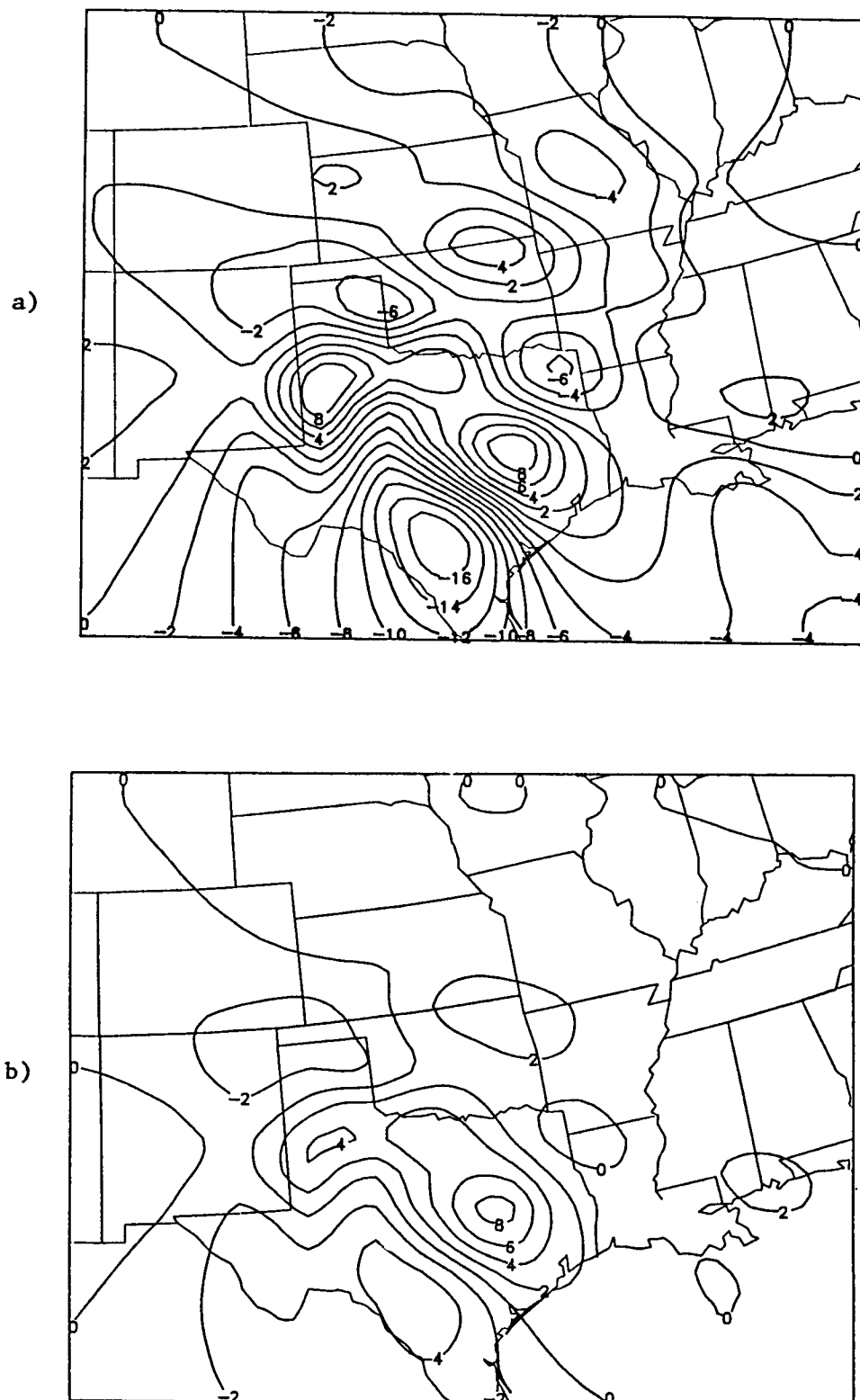


Fig. 2.1. Vertical velocity fields (cm/s) at 550 mb calculated with adiabatic method. Temperature tendencies are estimated by a) 6-hour centered difference and by b) Panofsky's approximation.

C. Variational Approach

The variational algorithms presented here are part of a more general diagnostic numerical model developed by Achtemeier (1975) and Achtemeier et al (1984, 1985, 1986b, 1986c). The model is set up on a Cartesian horizontal coordinate system and a pressure-sigma vertical coordinate system (Phillips, 1957; Shuman and Hovermale, 1968). This non-linear vertical coordinate, displayed in Fig. 2.2, is a terrain following system from the surface to a predetermined level, p^* . Above p^* , the vertical coordinate is coincident with constant pressure surfaces. Its selection is based on the simplicity of the boundary condition at the surface and on the computational ease at the pressure surfaces above p^* .

The equation relating the pressure coordinates to the sigma coordinates above p^* is

$$\sigma = \sigma^* \left(\frac{p - p_u}{p^* - p_u} \right) \quad (2.8)$$

where σ^* is $\sigma(p^*)$, p_u is the pressure at the top of the domain. For this work, p^* is 700 mb and p_u is 100 mb. The adiabatic equation of vertical velocity is provided by Eq. 2.6. Below p^* , this coordinate relationship is the cubic polynomial

$$\sigma = \beta(p - p^*)^3 + \sigma^* \left(\frac{p - p_u}{p^* - p_u} \right) \quad (2.9)$$

where,

$$\beta = \left[1 - \sigma^* \left(\frac{p_s - p_u}{p^* - p_u} \right) \right] (p_s - p^*)^{-3} \quad (2.10)$$

with p_s being the surface pressure. In this region, the adiabatic vertical velocity formulation, with R representing the gas constant for dry air, is

$$\dot{\sigma} = \left(\frac{\partial T}{\partial t} + \mathbf{v} \cdot \nabla_{\sigma} T \right) \left\{ \frac{RT}{c_p p} [3(p - p^*)^2 + \frac{\sigma^*}{p^* - p_u}]^{-1} - \frac{\partial T}{\partial \sigma} \right\}^{-1} \quad (2.11)$$

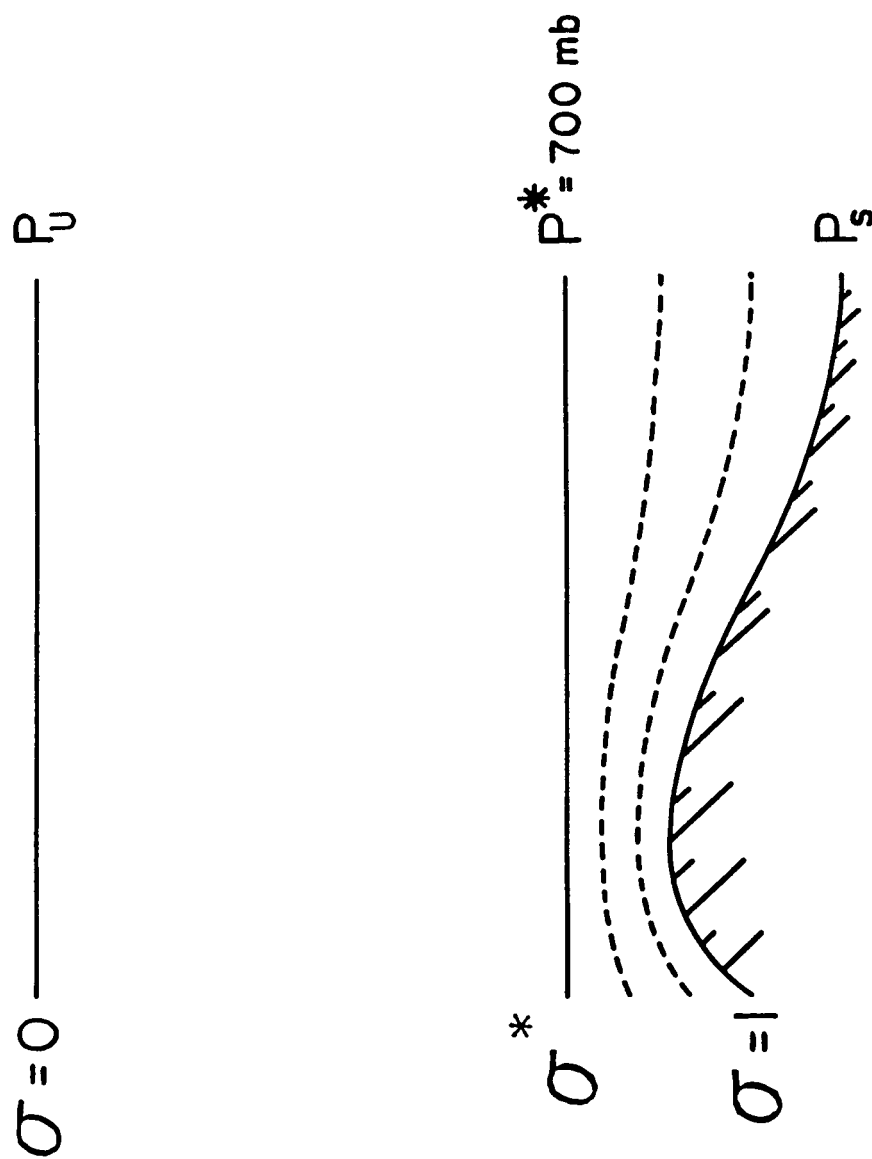


Fig. 2.2. Schematic of sigma-pressure coordinate system.

The variational algorithm for calculating vertical motion combines satellite data with conventional data. The conventional data are assigned weights according to their relative measurement accuracies. The satellite data are used to determine weights assigned to the independent, adiabatic estimate of vertical motion. The data are adjusted by a least squares approach that requires mass continuity to be satisfied.

The quantities to be minimized are contained in the function I , written for a nonlinear, sigma vertical coordinate.

$$I = \pi_1(u-u^\circ)^2 + \pi_1(v-v^\circ)^2 + \pi_2(\dot{\sigma}-\dot{\sigma}^\circ) + 2\lambda m \quad (2.12)$$

Here, π_1 and π_2 are the assigned weights, u° and v° are observed data, $\dot{\sigma}^\circ$ is the adiabatic estimate of vertical motion, λ is the Lagrange multiplier and m is the constraining continuity equation in sigma coordinates (Shuman and Hovermale, 1968). Symbolically,

$$m = \int Q \left(\frac{\partial u}{\partial x} + \frac{\partial v}{\partial y} \right) d\sigma + \dot{\sigma} - Q_0 \dot{\sigma}_0 + \int Q F d\sigma = 0 \quad (2.13)$$

where $\dot{\sigma}_0 = \dot{\sigma}$ at the surface, F is a function including the surface vertical velocity and factors to transform the equation to a Lambert conformal map image projection, and Q is a fractional quantity related to the pressure thickness of a layer.

Subjecting I to the Euler-Lagrange operations (Sasaki, 1958) and setting the results to zero, allows the quantities u , v , and $\dot{\sigma}$ to be minimized.

$$\delta u = \pi_1(u-u^\circ) - \frac{\partial \lambda}{\partial x} = 0 \quad (2.14)$$

$$\delta v = \pi_1(v-v^\circ) - \frac{\partial \lambda}{\partial y} = 0 \quad (2.15)$$

$$\delta \dot{\sigma} = \pi_2(\dot{\sigma}-\dot{\sigma}^\circ) - \lambda = 0 \quad (2.16)$$

The error variance of the horizontal wind measurements is assumed to vary only with height and from the formulation of the continuity equation, Eq. 2.13, λ is a function of only the horizontal coordinates. Then, Eqs. 2.14 and 2.15 can be differentiated and combined with 2.16 to solve for λ . Here, λ is expressed in the form of a Helmholtz equation:

$$b\nabla^2\lambda - a\lambda + H = 0 \quad (2.17)$$

where

$$b = \int_{\sigma_0}^{\sigma_1} Q / \pi_1 d\sigma \quad (2.18)$$

$$a = [\pi_2 \int_{\sigma_0}^{\sigma_1} Q d\sigma]^{-1} \quad (2.19)$$

and

$$H = \dot{\sigma}^\circ - Q_0 \dot{\sigma}_0 + \int_{\sigma_0}^{\sigma_1} Q (F + \partial u^\circ / \partial x + \partial v^\circ / \partial y) d\sigma. \quad (2.20)$$

The determination of the variationally adjusted vertical motion is a two-step process. First, with the version of the Barnes (1973) scheme mentioned in Appendix A, the observed u and v components are interpolated to a 24 by 20 grid at ten levels. From these fields, the kinematic vertical velocities and the corresponding adjusted horizontal divergences are obtained using O'Brien's (1970) method with the surface vertical velocity determined by

$$\omega_s = dp_s/dt = \partial p_s / \partial t + \vec{V} \cdot \nabla p_s. \quad (2.21)$$

Second, the kinematically adjusted u and v components become the "observed" quantities in the function to be minimized. A solution is obtained for the Lagrange multiplier using a successive over-relaxation technique (Forsythe and Wasow, 1960), and the vertical velocity is found from the constraining equation, Eq. 2.13. There are three quantities

which determine the final vertical velocity value: the average O'Brien adjusted horizontal divergence of the layer, the adiabatic estimate, and the variational result calculated for the layer below. These final values of $\dot{\sigma}$ can be converted to pressure coordinate vertical velocities by using

$$\omega = \frac{Z}{J} \dot{\sigma} + \frac{J_S}{J} \left(\frac{Z}{Z_S} \right)^4 \omega_S ; \quad p > p^* \quad (2.22)$$

$$\omega = \dot{\sigma} / \alpha ; \quad p \leq p^* \quad (2.23)$$

where

and

$$z = p - p^*$$

$$z_S = p_S - p^*$$

$$\alpha = \frac{\sigma^*}{p^* - p_u}$$

$$J = 3\beta z^3 + \alpha z$$

$$J_S = 3\beta z_S^3 + \alpha z_S .$$

1. Determination of Weights

The Gauss precision moduli, π_1 and π_2 are weights accorded to the divergences of the horizontal wind, which when vertically integrated, yield O'Brien corrected kinematic vertical velocities and to the adiabatic estimates of vertical velocity, respectively. More influence is given to that method which is physically more applicable. Namely, the kinematic values are given greater weight in regions of diabatic heating such as cloudy layers and near the surface and in neutrally stable layers. More weight is supplied to the adiabatic method in clear or very stable layers.

The weight π_1 is determined from the relative rawinsonde measurement errors in the horizontal velocity. These are listed in

Table 2.1 (Achtemeier et al, 1986c). The value of π_1 is calculated as in Eq. 2.3.

<u>P(mb)</u>	<u>RMSE_v (m/s)</u>
100	4.5
200	4.5
300	4.2
400	3.6
500	3.2
600	3.0
700	2.8
800	2.4
900	2.1
1000	2.0

Table 2.1. Root mean square error (RMSE) of observed horizontal velocities.

The second weight, π_2 , incorporates three factors in its formulation: 1) error variance of the adiabatic vertical velocity obtained from its approximation by measured quantities, 2) cloudiness along with relative humidity, and 3) static stability parameter, s . From these factors, criteria are set so that there is physical agreement between prevailing weather conditions and the adiabatic assumption.

A sensitivity test is performed to determine bounds on the value of π_2 . The u and v components of one case period, 12Z 10 April, are used to develop an O'Brien kinematic vertical velocity field. The adiabatic vertical velocity field is set identically to 0. The value of π_2 is increased until the resulting w field is not significantly different from the adiabatic field. Likewise, the value of π_2 is decreased until the resulting w field is not significantly different from the kinematic w field. The bounds on π_2 are found to be 10^{-2} and 10^{+2} .

The contribution from each factor to the determination of the weight is assumed to be linear with the logarithm of π_2 . The range of values that each contributing factor may take on is scaled from -2 to +2. Thus, the value of π_2 is the anti-logarithm of a linear combination as described by Eq. 2.24.

$$\pi_2 = 10^{1/3(A + B + C)} \quad (2.24)$$

Here, A is a value representing the contribution of the measurement error, B is a value determining the contribution of cloudiness and moisture, and C is a value representing the contribution of the stability parameter.

The development of the error variances for the adiabatic vertical velocity is provided in Appendix B. The precision moduli are determined as described before in Eq. 2.3.

The cloudiness is determined using GOES infrared data and relative humidity fields which are derived from rawinsonde soundings. The infrared data are converted to cloud top temperatures (Gibson et al, 1984). Each point in the 24 by 20 grid is assigned the temperature value which is the average of a box, seven pixels on a side, centered on that point. Any "questionable" pixel whose value is much different from that of its neighbors is disregarded. A threshold of -20 C is set as a cloud top temperature which could indicate a region of significant cloud development. This temperature cut off is described by Griffith et al (1978) as a value which could identify precipitation producing clouds. Any grid point with a value greater than -20 C is assigned 0 in the cloudiness array and the remaining points assigned a value of 1.

Relative humidity data are used to give a height dimension to the two-dimensional cloudiness array. For any cloudiness point defined as 1, the relative humidity must be at least 60% for a given layer or the value is reset to 0 at that layer. Any point which displays a relative humidity value greater than 90% is defined as 1. This array is smoothed with a filter to eliminate the abrupt step in the field while values assigned as 1 retain that value. This array is then scaled linearly such that a cloudiness value of 0 corresponds to 2 and a value of 1 corresponds to -2.

The final factor is the static stability parameter. A major disadvantage to the adiabatic method is that the estimate of vertical velocity "blows up" for near neutral lapse rates where s approaches 0. A lower threshold value for s of 20 K/layer or about 2K/100 mb is set. This value was also used by Fuelberg and Lee (1983). An upper bound for s of 100 K/layer or about 11 K/100 mb is also set. This value is determined from observations of fields of static stability parameter for all cases studied in this work. In the stability array, grid points with values less than 20 K/layer are set to 0 and grid points with values greater than 100 K/layer are defined as 1. The intermediate s values are empirically given values according to

$$C = e^{-\left(\frac{s-50}{12}\right)^2} ; s \leq 40\text{K/layer} \quad (2.25)$$

$$C = 1 - .5e^{-\left(\frac{s-40}{12.5}\right)} ; s > 40\text{K/layer} \quad (2.26)$$

These piecewise continuous curves are selected such that the mean s value receives about 50% weight and such that s values just larger than 20 K/layer receive very little weight and those slightly smaller than

100 K/layer receive a weight of nearly 1. As with the cloudiness array, the stability is linearly scaled but with 0 corresponding to -2 and 1 corresponding to 2.

Instead of a simple average exhibited by Eq 2.24, a weighted average is employed. This allows the contribution of the terms to be increased or diminished according to physical conditions. The form of this expression of appears in Eq. 2.27.

$$\pi_2 = 10 \left(\frac{aA + bB + cC}{a + b + c} \right) \quad (2.27)$$

where a, b, and c are the weighting coefficients multiplied to the terms, A, B, and C, respectively. Since many assumptions are used in developing the error variance of w, it is given least weight. The coefficient for error variance is set to a constant value of 0.25. Any relative humidity values greater than 90% provide additional influence for the cloudiness array because for very moist conditions the kinematic method should dominate. When this criteria is met, the coefficient is set to a constant value of 50. This quantity is selected such that extreme values of stability parameter may override the contribution by cloudiness and moisture. Stability parameters near zero are weighted to insure that the kinematic method dominates, and extremely stable layers are given extra weight to override any cloudiness. Therefore, any values of s less than 20 K/layer or any values greater than 85 K/layer increase the static stability contribution. This is done by defining empirical functions to assign the coefficient. These functions are provided in Eqs. 2.28 and 2.29.

$$c = .100 e^{\left(\frac{C - 1}{.3}\right)^2} \quad ; \quad s \leq 20K/layer \quad (2.28)$$

$$c = 100 e^{\left(\frac{C}{.3}\right)^2} \quad ; \quad s \geq 85K/layer \quad (2.29)$$

Finally, the weighted average of the three factors is determined. The value of π_2 is the anti-logarithm of the average.

The fields of π_2 prove to be very noisy, and the fields are smoothed before incorporating them in the variational algorithm. The smoothing technique employed in the interior of the field is the sinusoidal function (Oppenheim and Schafer, 1975)

$$Q_{i,j} = \frac{\sum_{q=0}^3 \sum_{r=0}^3 f_{qr} Q_{i+q,j+r}}{\sum_{q=0}^3 \sum_{r=0}^3 f_{qr}} \quad (2.30)$$

where

$$f_{qr} = \frac{1}{2} [1 - \cos(\frac{3-n}{3}\pi)]$$

where Q_L is a quantity at point i,j and n is a distance in grid space units. A line integral scheme is used around the edge.

$$Q_L = \frac{Q_{L-2} + 4Q_{L-1} + 6Q_L + 4Q_{L+1} + Q_{L+2}}{16} \quad (2.31)$$

Here, L refers to i along the east-west edges and to j along the north-south edges.

CHAPTER III

DATA AND SYNOPTIC AND MESOSCALE CONDITIONS

The data used to test the variational vertical velocity algorithm is from the first case period of the AVE-SESAME. This study spanned the period of 12Z 10 April - 12Z 11 April 1979. Alberty *et al* (1980) report that during this time, 89 severe weather events including four killer tornadoes occurred. This data set is chosen, not for its eventfulness, but rather for the increased density, for the frequency of rawinsonde observations with coincident satellite measurements, and for its vast documentation.

The area of this experiment was concentrated in the Central and South Central United States. Sixteen supplemental rawinsonde sites were set up to be used in addition to the regularly existing National Weather Service sites. Fig. 3.1 displays the domain used in this work with rawinsonde sites noted. The dashed line borders the data-rich region, and results obtained outside this region should be considered invalid. Observations were conducted every three hours. Table 3.1 lists the number of reporting stations for each time period.

<u>Observing Time</u>	<u>No. of Reporting Stations</u>
10 April 12Z	34
15Z	37
18Z	36
21Z	36
11 April 00Z	35
03Z	38
06Z	34
09Z	35
12Z	34

Table 3.1.- Number of rawinsonde stations reporting during AVE-SESAME I.

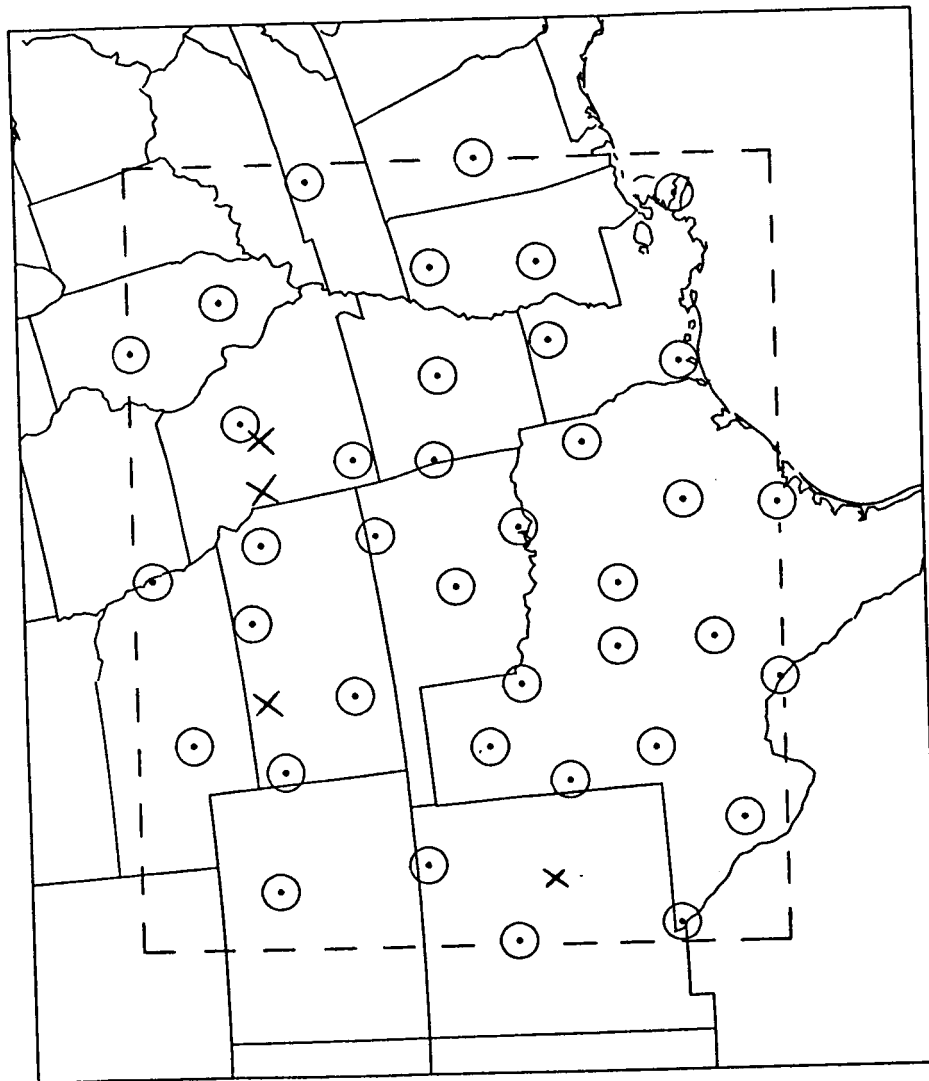


Fig. 3.1. Domain for data set of AVE-SESAME 1. Bullseyes denote locations of observations, x's denote locations of vertical velocity profiles, and dashed lines enclose data-rich region.

Six variables are extracted from the data set for this study. They are pressure, temperature, wind speed, wind direction, mixing ratio and geopotential height. The wind speed and direction are converted to x and y components, and the relative humidity is calculated from the mixing ratio. These observations are analyzed onto a gridded field by the aforementioned version of the Barnes (1973) objective analysis scheme. This field is a 24 by 20 point Cartesian grid overlying a Lambert conformal map projection image. One grid space unit is 100 km. The origin of the grid is 27° N, 110° W with the western border lying along 110° W.

The horizontal components of velocity are staggered by one-half grid space. Divergence is found for the center of a grid square, and vertical motion is located directly above the divergence at one-half the layer pressure thickness. (Refer to Fig. 3.2.) All tendencies are calculated using centered time differences, except the first and last time periods which use uncentered differences.

Descriptions of the synoptic and mesoscale conditions are provided by many sources (eg., Moore and Fuelberg, 1981; Carlson et al, 1980; Vincent and Homan, 1983; Homan and Vincent, 1983). The following is a summary of the prevailing conditions.

At the surface during most of the time in question, the eastern half of the United States was under the influence of high pressure and experiencing cool, dry conditions. A low pressure center was anchored in Colorado and remained at nearly the same location and intensity.

According to Moore and Fuelberg (1981), at 12Z 10 April moist air from the Gulf of Mexico was being advected over southern Texas in lower levels, and a dry line was developing over western Texas. At 700 mb,

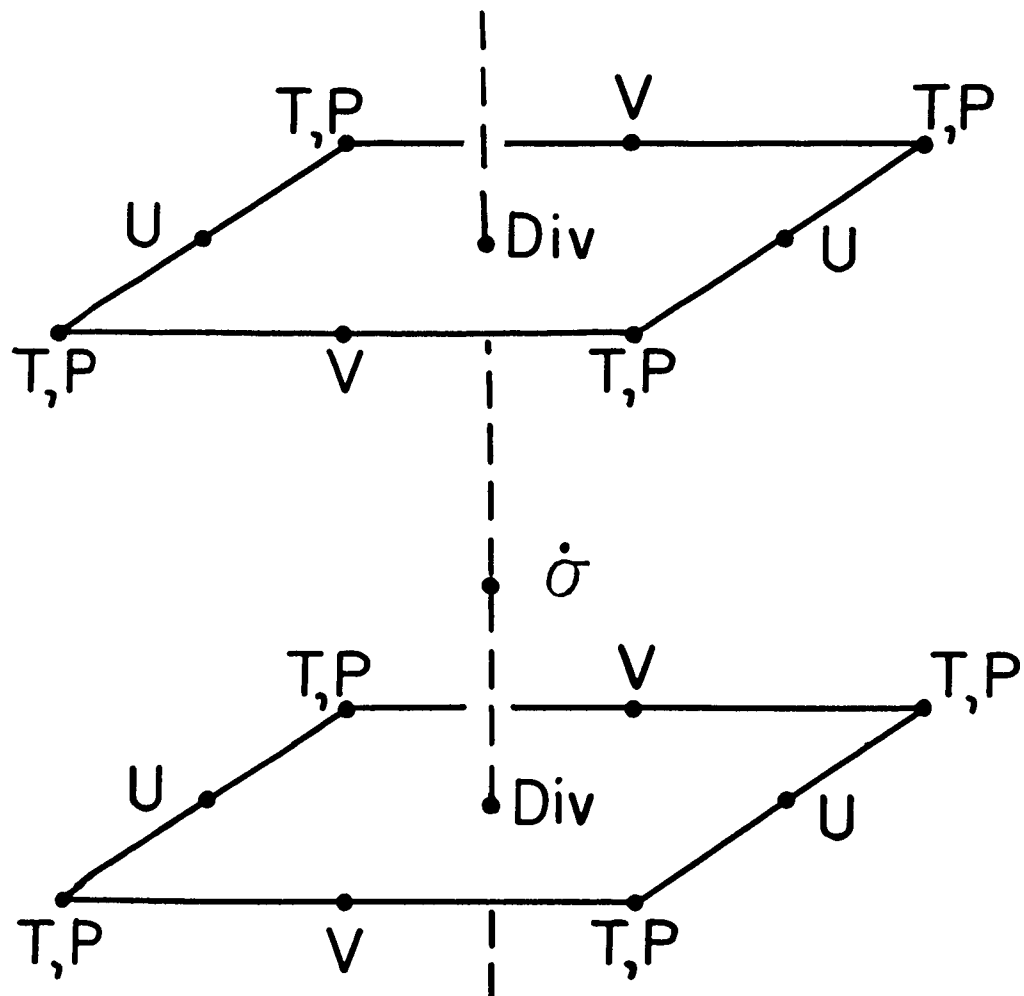


Fig. 3.2. Schematic of variable locations upon grid.

southwesterly flow brought dry air to overlie the moist air at the Red River Valley. An amplifying wave extending from Washington to New Mexico appeared at 300 mb along with a weakening short wave over the Midwest. Also at 300 mb, there is a jet streak over northern Mexico.

By 18Z 10 April, this jet streak is located just west of a short wave trough. Moore and Fuelberg believe that the propagation of this upper level jet streak played a major role in the Red River Valley tornado outbreak. They associate this jet streak with the formation of a strong low level jet and small-scale surface pressure perturbations. This theory is supported by Vincent and Homan (1983). They used barograph traces to locate two meso-low centers. One of these mesolows developed in the Texas panhandle at 19-20Z 10 April and moved slowly eastward intensifying at 20-22Z. Another meso-low system occurred in north central Texas at 1-2Z 11 April.

CHAPTER IV

RESULTS

A. Vertical Velocity Results: Horizontal Fields

O'Brien adjusted kinematic, adiabatic, and variational vertical velocities are calculated for each time. Presented for this study are 12Z and 18Z (10 April) and 0Z and 6Z (11 April). These times are selected so that the two middle times, 18Z and 0Z, are within the period of severe storm activity and the remaining times, 12Z and 6Z, represent pre-storm and post-storm conditions, respectively. The displayed fields are for the 450 mb and 150 mb levels.

The 12Z results for the kinematic method are shown in Fig. 4.1. At 450 mb, there exists a band of intense upward motion lying across upper New Mexico and stretching northeastward to northwest Kansas. A region of upward motion is found at northern Mississippi and Alabama. Most of the Midwest is experiencing downward motion, and a localized area of subsidence is present over southeast Oklahoma. At the 150 mb level, very intense regions of upward motion occur over New Mexico (magnitudes greater than 20 cm/s), over the Nebraska-Kansas border and southwestern Texas. Intense centers of sinking motion are evident over Iowa, the Texas panhandle and central Texas.

The adiabatic motion fields for 12Z appear in Fig. 4.2. Here, at 450 mb, upward motion is found over northern Colorado, the Texas panhandle, and the Missouri-Arkansas border. Downward motion is noticed over eastern Oklahoma and Kansas. At the 150 mb level, weak rising motion is present in two bands: one extending from eastern Texas through central Oklahoma and Kansas and into northern Missouri and another from eastern Louisiana through Mississippi and into central Texas.

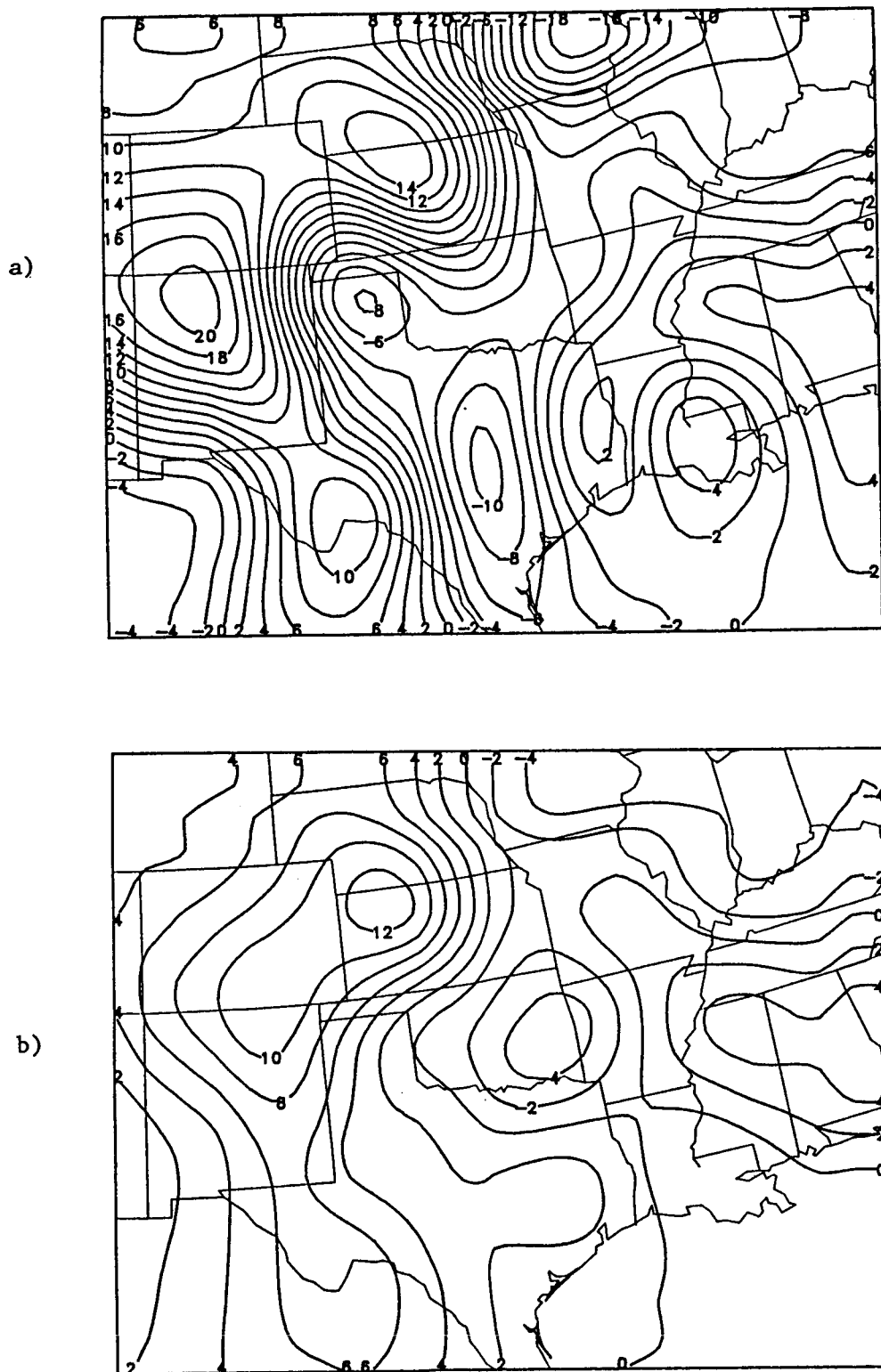


Fig. 4.1. Vertical velocity fields (cm/s) for 12Z 10 April 1979 calculated by the O'Brien adjusted kinematic method at a) 150 mb and b) 450 mb.

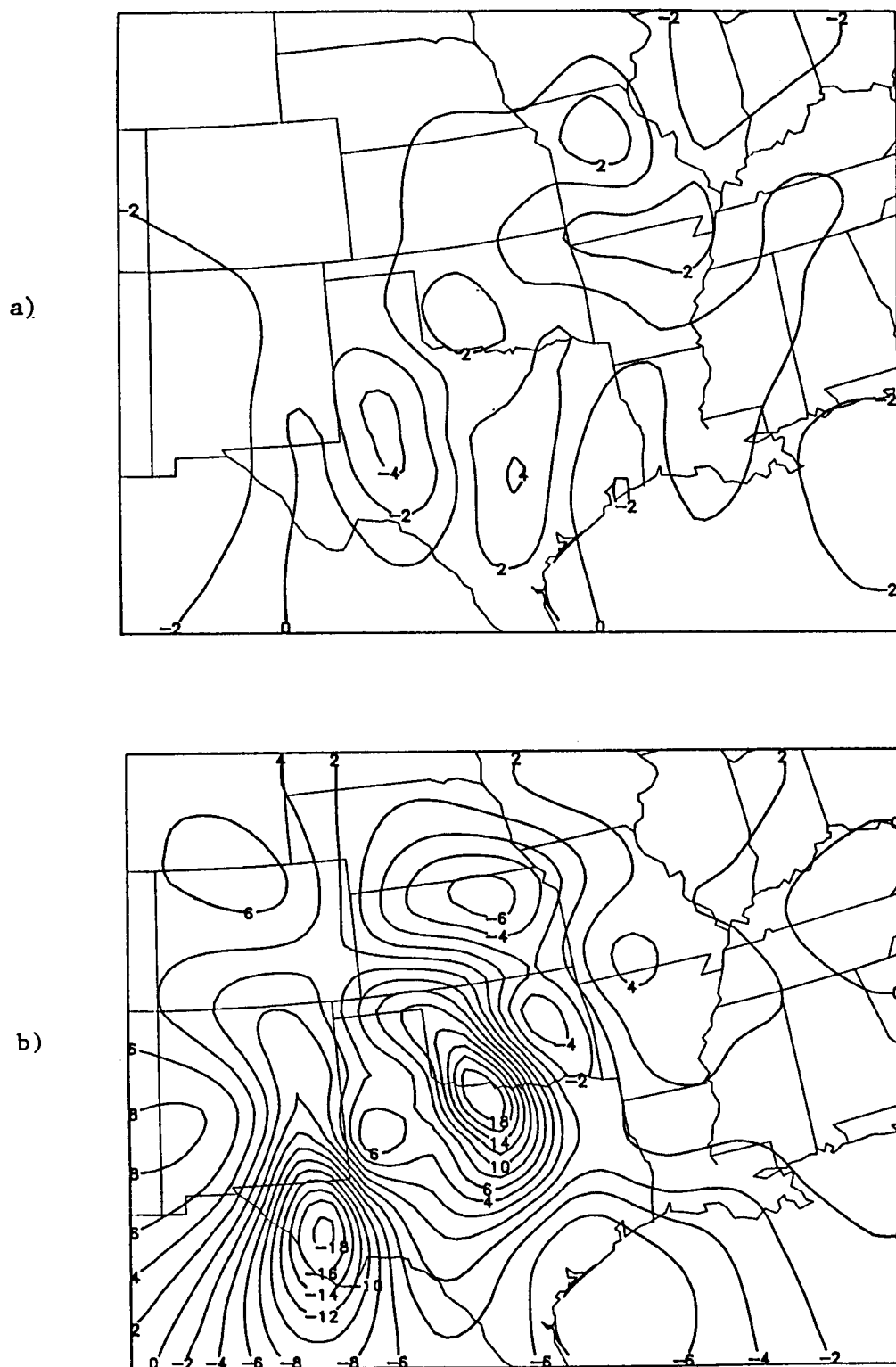


Fig. 4.2. Vertical velocity fields (cm/s) for 12Z 10 April 1979 calculated by the adiabatic method at a) 150 mb and b) 450 mb.

Except for the subsidence over eastern Oklahoma, the two vertical velocity fields at 450 mb show little resemblance. The kinematic pattern compares well with the field of largely non-precipitating clouds over Kansas, Colorado, and New Mexico. The upward adiabatic vertical velocity center over central Texas at 450 mb is associated with strong warm advection with little compensating temperature change. Similarly, the sinking adiabatic center over southwestern Texas is related to strong cold air advection with small compensating temperature tendency. The relatively small magnitudes of adiabatic vertical velocity at 150 mb are indicative of the stable lapse rates of the lower stratosphere.

The field of weighting factor, π_2 , is displayed in Fig. 4.3. The field is contoured using the logarithm of the value. Positive valued contours represent areas where adiabatic method is receiving more weight, and negative values indicate that the O'Brien corrected horizontal divergences are given a stronger influence. The contributing factors of stability and of cloudiness with relative humidity are shown in Fig. 4.4. The stability field, Fig. 4.4a, exhibits areas of near neutral lapse rates over the Red River Valley and in extreme southwestern Texas. The field in Fig. 4.4b shows that diabatic processes such as latent heating may be present in western New Mexico and western Colorado and in a band across Kansas and Missouri. In these regions, the adiabatic method should receive small influence. The GOES infrared image exhibited in Fig. 4.5 shows a lack of cold cloud top temperatures over Texas and northern Louisiana. This is possibly due to the absence of moisture in the upper layers even though upward motion exists. Another clear area is prevalent over Oklahoma due to subsidence. The cold cloud tops over the Midwest are probably high cold

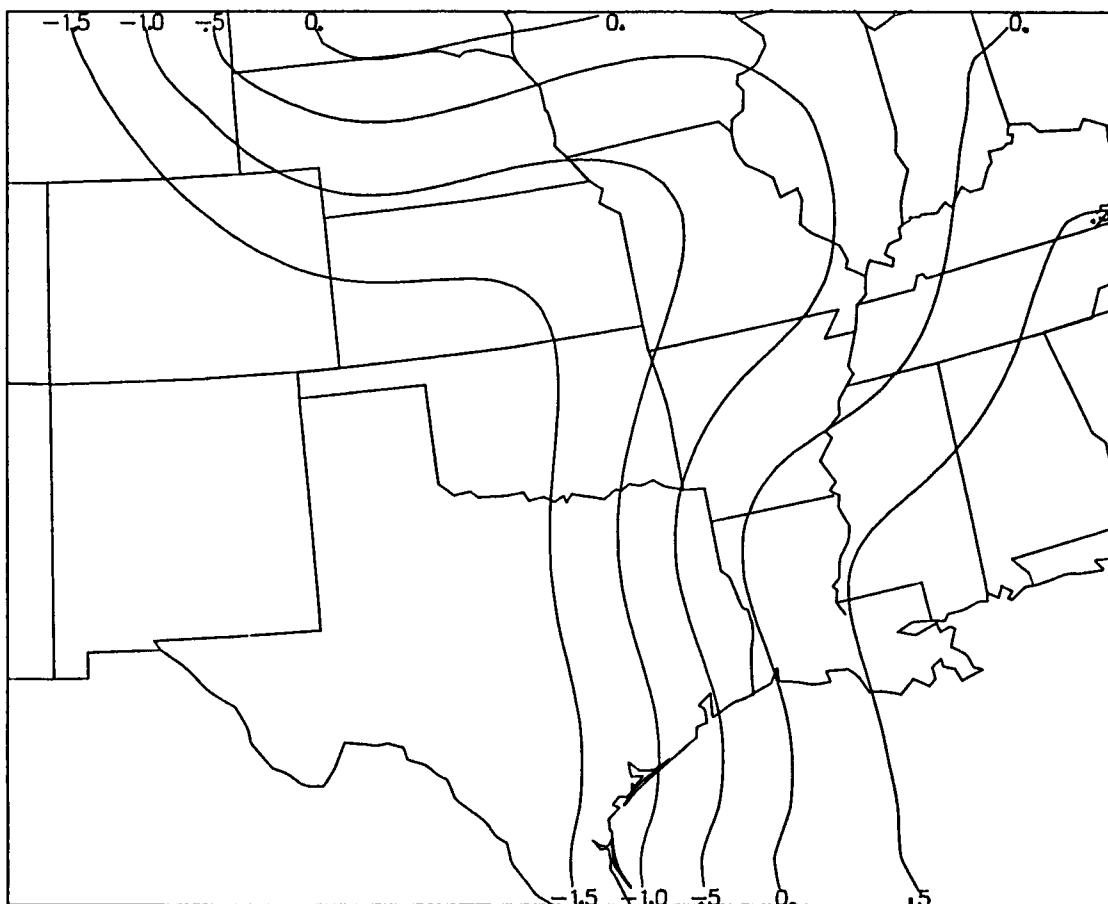


Fig. 4.3. Field of $\log(\pi_2)$ for 12Z 10 April 1979 at 450 mb.

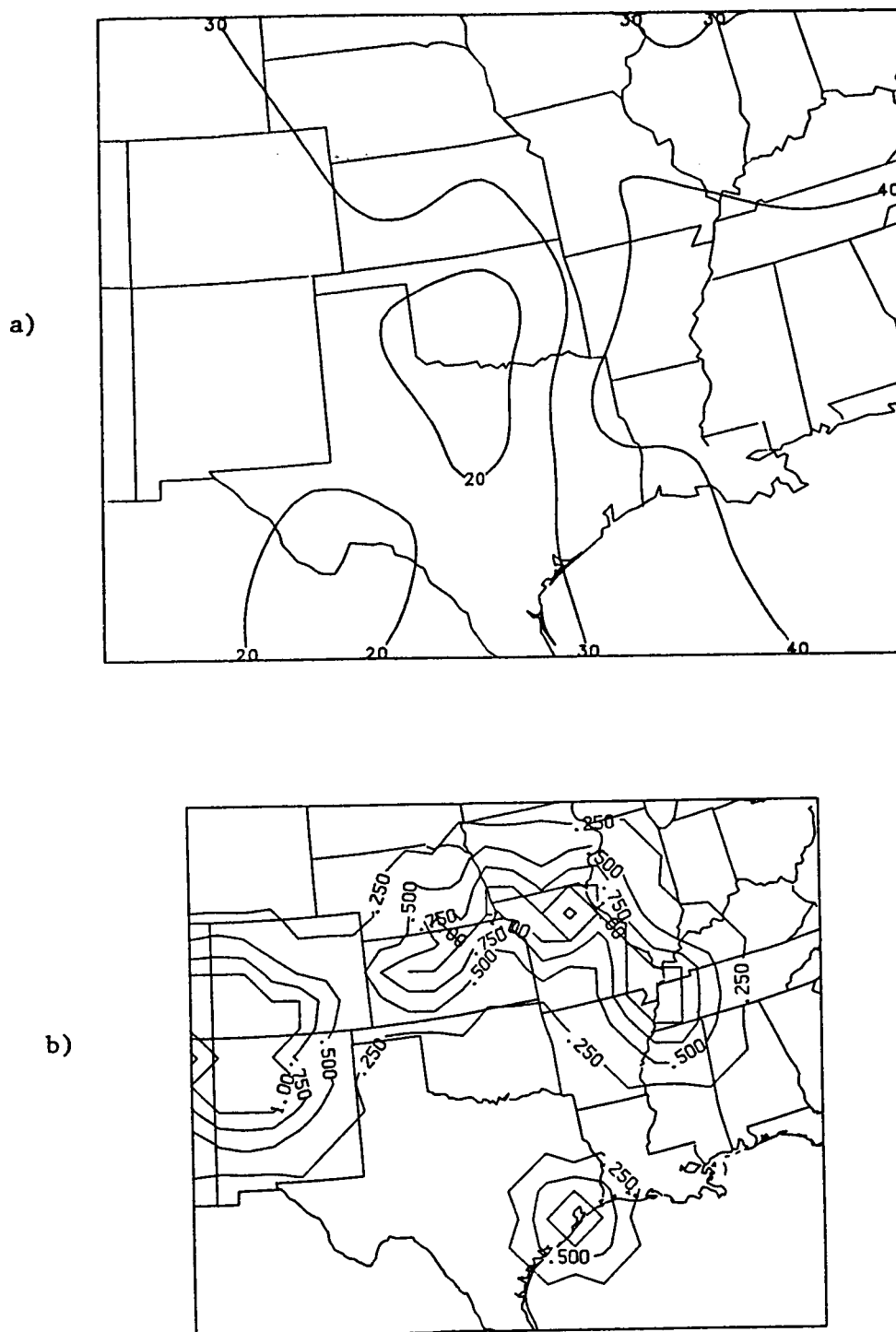


Fig. 4.4. Fields of a) static stability parameter (K/layer) and b) clouds with relative humidity for 12Z 10 April 1979 at 450 mb.

ORIGINAL PAGE IS
OF POOR QUALITY

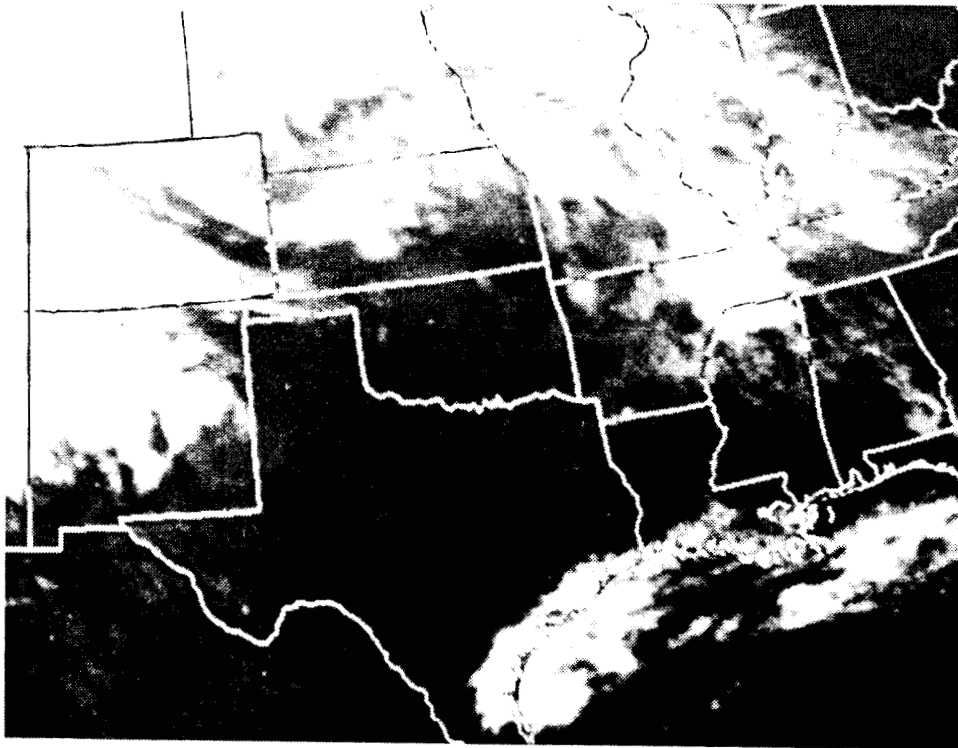


Fig. 4.5. GOES infrared image for 1230Z 10 April 1979.

cirrus clouds since there is low relative humidity in the middle layers. This is reflected in the weighting function, Fig. 4.3, since increasing influence is given to the adiabatic estimate in that region.

In Fig. 4.6 are the resulting variational vertical motion fields. At 450 mb, the isoline of $\pi_2 = 10^0$ is depicted on the velocity field. It is along this contour that the adiabatic estimate and the average horizontal divergence assume nearly equal weight. Noticeable features of the variational field are that 1) the band of upward motion over northeast New Mexico into Colorado and northeast Kansas which appeared in the kinematic field are restored with decreased magnitude, 2) a large region of subsidence is present over the Midwest with centers in southern Iowa and the southeast corner of Oklahoma, and 3) a band of upward motion expands eastern Texas and through the southern Mississippi Valley states. Maxima are present in eastern Texas and northern Mississippi. The layer at 150 mb is quite stable. Consequently, the adiabatic estimate dominates and the variational field is approximately the same as the adiabatic field.

The precipitation echoes from the 1135Z radar summary are traced onto the variational velocity field at 450 mb. From these echoes light and scattered rain showers through Kansas and Arkansas, and rain showers in central New Mexico can be detected. A small localized thunderstorm with 11 km cloud tops appears at the Texas-Louisiana border.

The kinematic vertical motion fields for 18Z are displayed in Fig. 4.7. At 450 mb, an intense maximum (greater than 14 cm/s) is positioned over northeast New Mexico. The scenario for most of the western regions of the grid and the Plains states is rising motion with a cut off minimum in west central Texas. Sinking motion is organized in

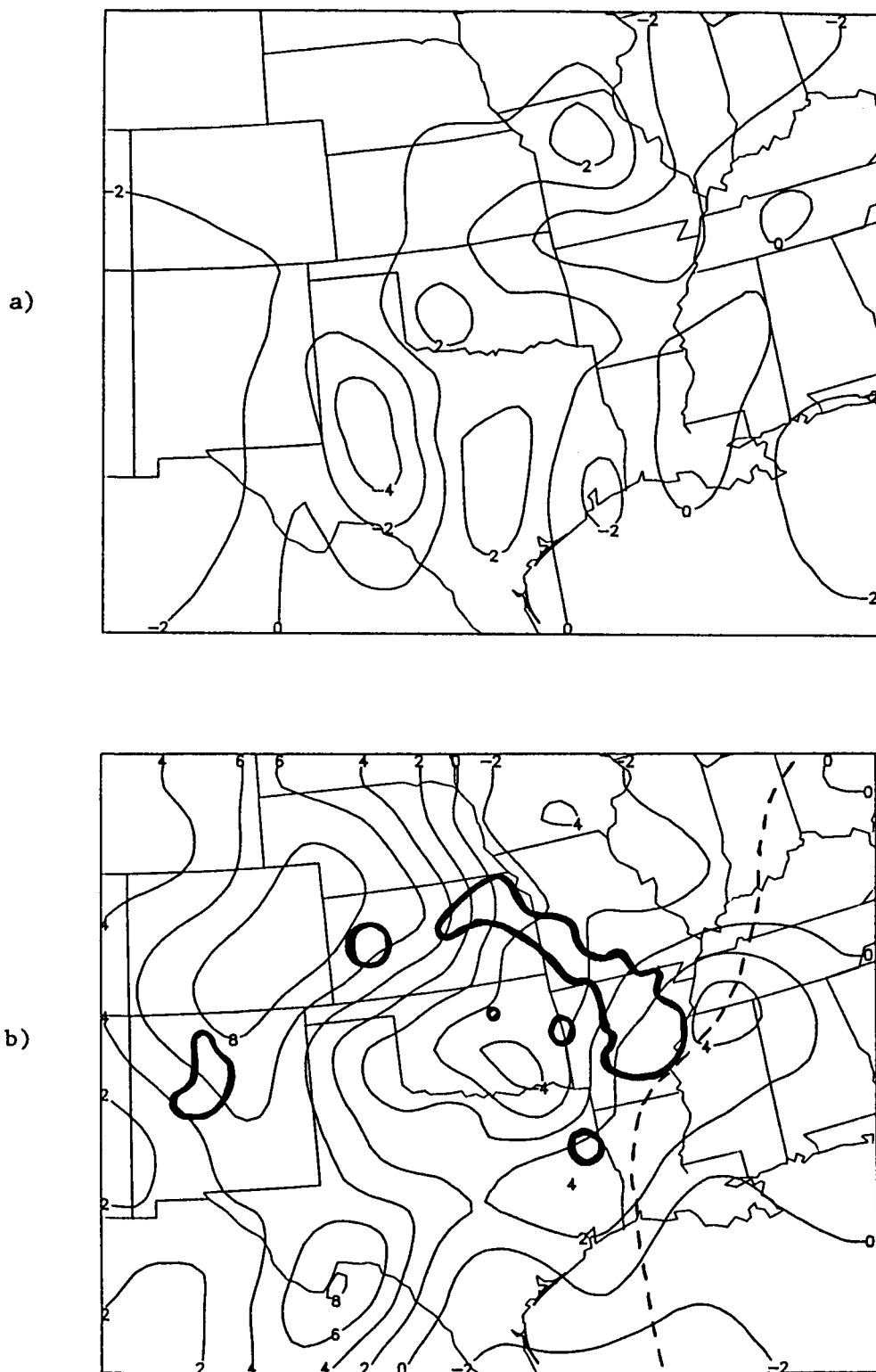


Fig. 4.6. Vertical velocity fields (cm/s) for 12Z 10 April 1979 calculated by the variational algorithm at a) 150 mb and b) 450 mb. In b), bold lines indicate precipitation echoes taken from radar summary and dashed line is $\pi_2 = 10^0$ contour.

a band reaching from Arkansas into the Midwestern states. At 150 mb, two maxima of upward motion are noticed. One center is over northern New Mexico with a magnitude greater than 20 cm/s and another is over southwest Missouri with a magnitude greater than 10 cm/s. A band of subsidence having a values less than -6 cm/s stretches through southern Oklahoma and western Texas.

Features of the adiabatic estimation shown in Fig. 4.8 include upward motion just south of the Red River Valley and in eastern Louisiana. Sinking motion is found at the Texas panhandle, at the Texas-Arkansas border, and in a band extending through Iowa, Missouri and northern Arkansas. The 150 mb level shows mostly weak upward motion located in the southwest section of the grid with the exception of an area in western Texas. The northern region of the grid generally exhibits sinking motion with an extreme in northeast Arkansas.

The field of weighting function for 18Z is displayed in Fig. 4.9. As before, negative areas indicate greater influence by the O'Brien corrected horizontal divergences and positive areas are locations of adiabatic influence. This field shows that almost the entire grid, except for a small area in Alabama and Mississippi which is outside the data-rich region, gives more weight to the adjusted divergences. In Fig. 4.10, the contributing factors to the weighting factor at 450 mb are shown. The stability field of Fig. 4.10a includes a large region in west central Texas and a smaller region at the Oklahoma-Arkansas border which are areas of near neutral lapse rate. In these regions, kinematic vertical velocities are accorded the larger weighting. Cold cloud tops seen in the GOES infrared image, Fig. 4.11, are supported with sufficient moisture at 450 mb in the locations of northern New Mexico,

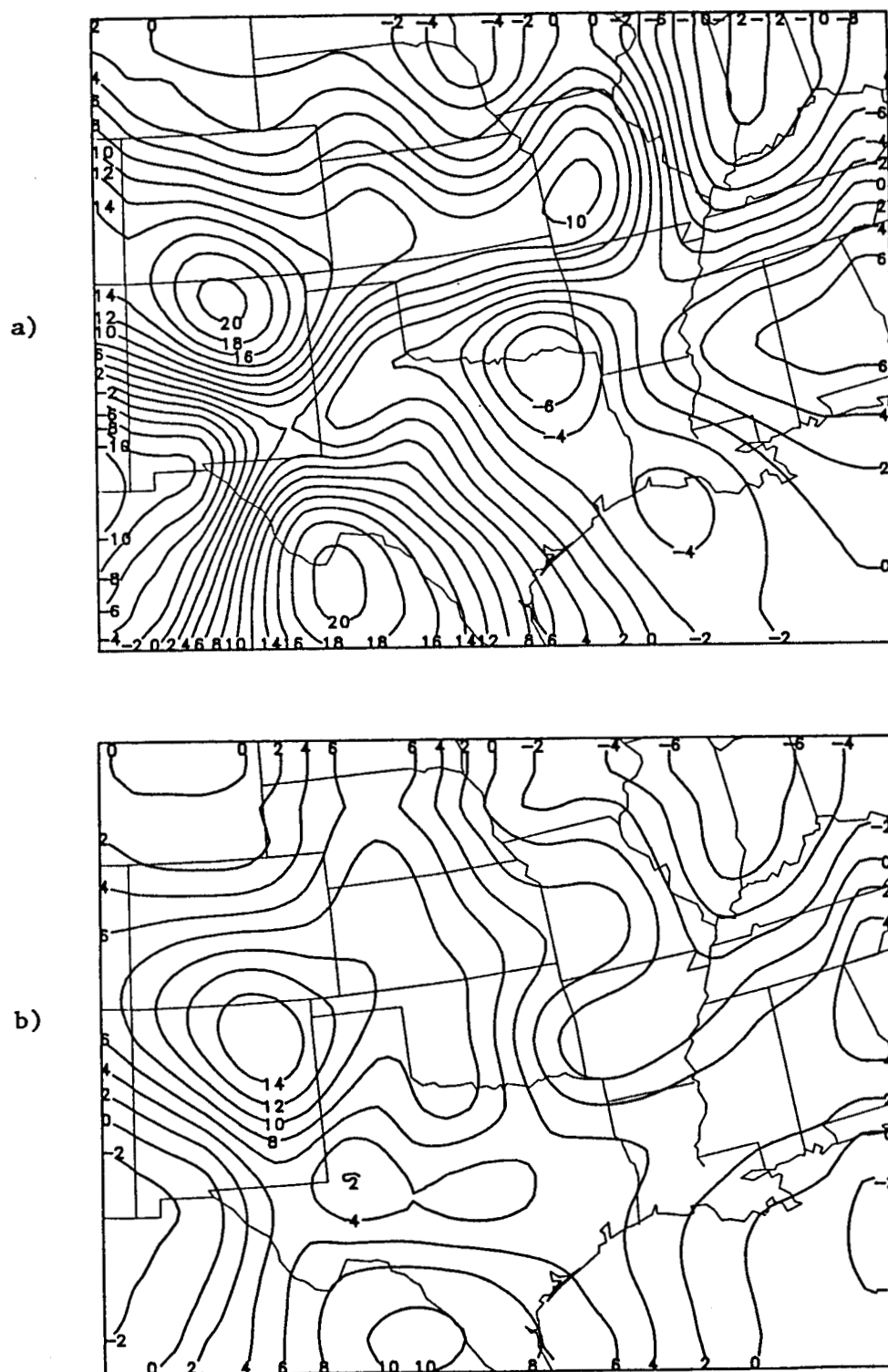
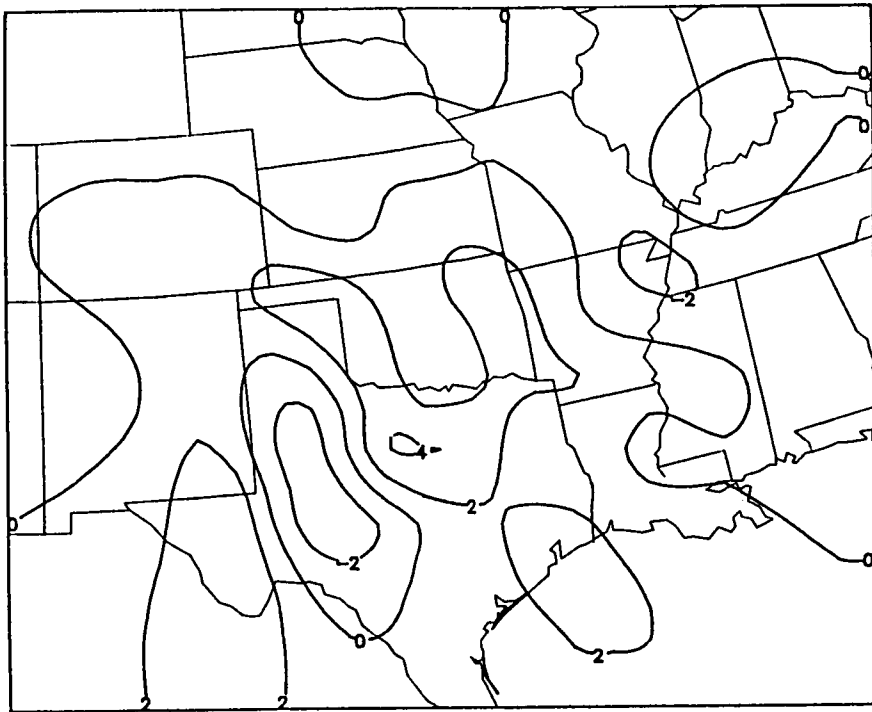


Fig. 4.7. Vertical velocity fields (cm/s) for 18Z 10 April 1979 calculated by the O'Brien adjusted kinematic method at a) 150 mb and b) 450 mb.

a)



b)

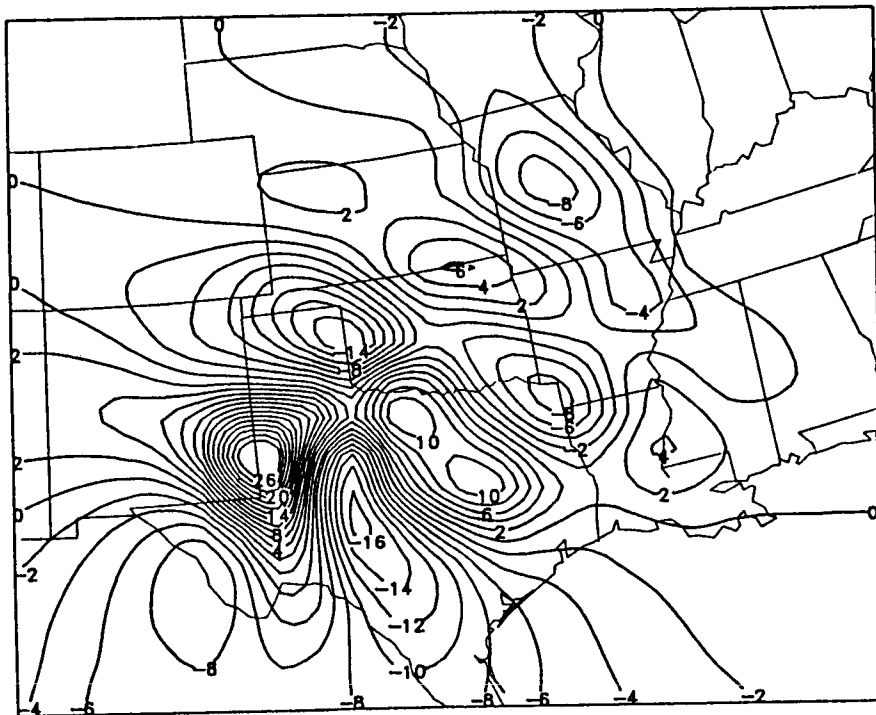


Fig. 4.8. Vertical velocity fields (cm/s) for 18Z 10 April 1979 calculated by the adiabatic method at a) 150 mb and b) 450 mb.

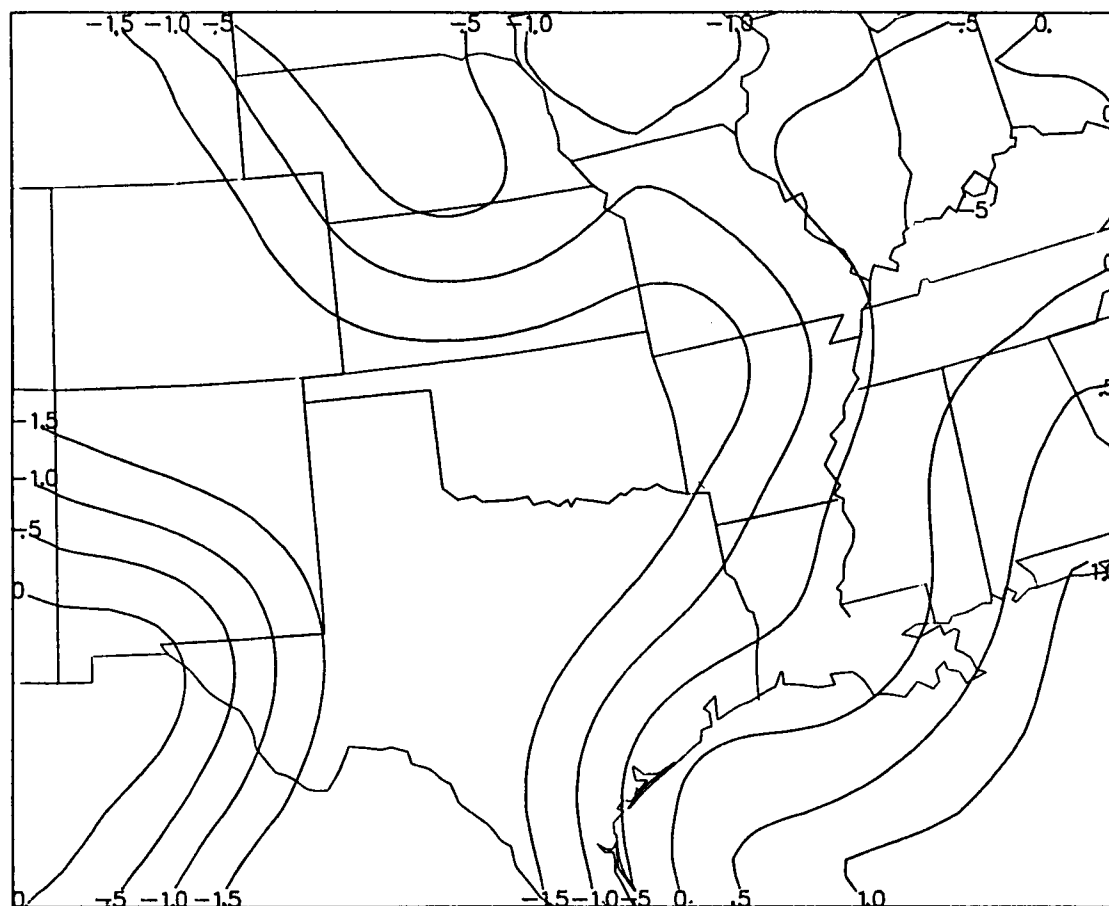


Fig. 4.9. Field of $\log(\pi_2)$ for 18Z 10 April 1979 at 450 mb.

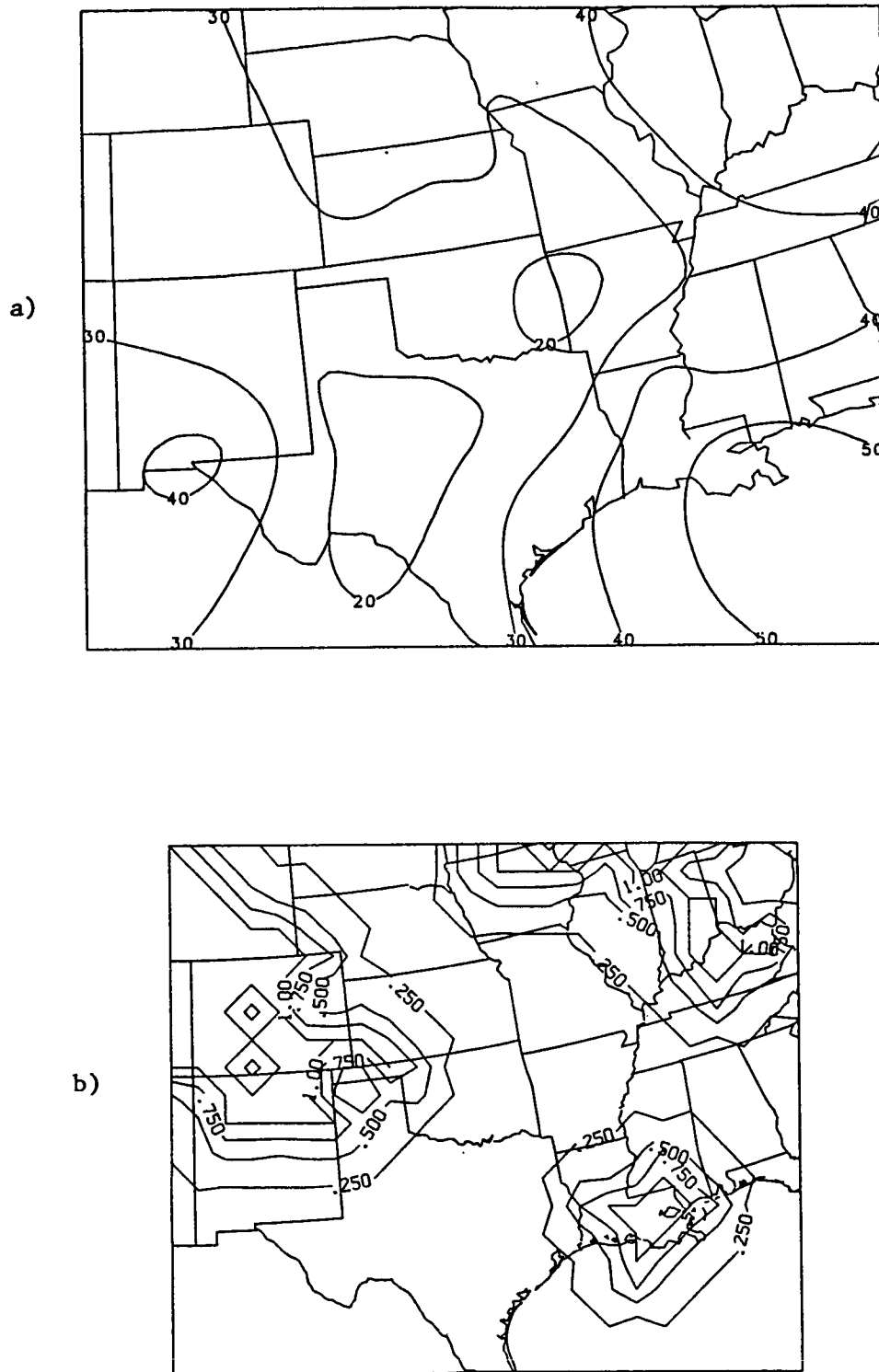


Fig. 4.10. Fields of a) static stability parameter (K/layer) and b) clouds with relative humidity for 18Z 10 April 1979 at 450 mb.

ORIGINAL PAGE IS
OF POOR QUALITY

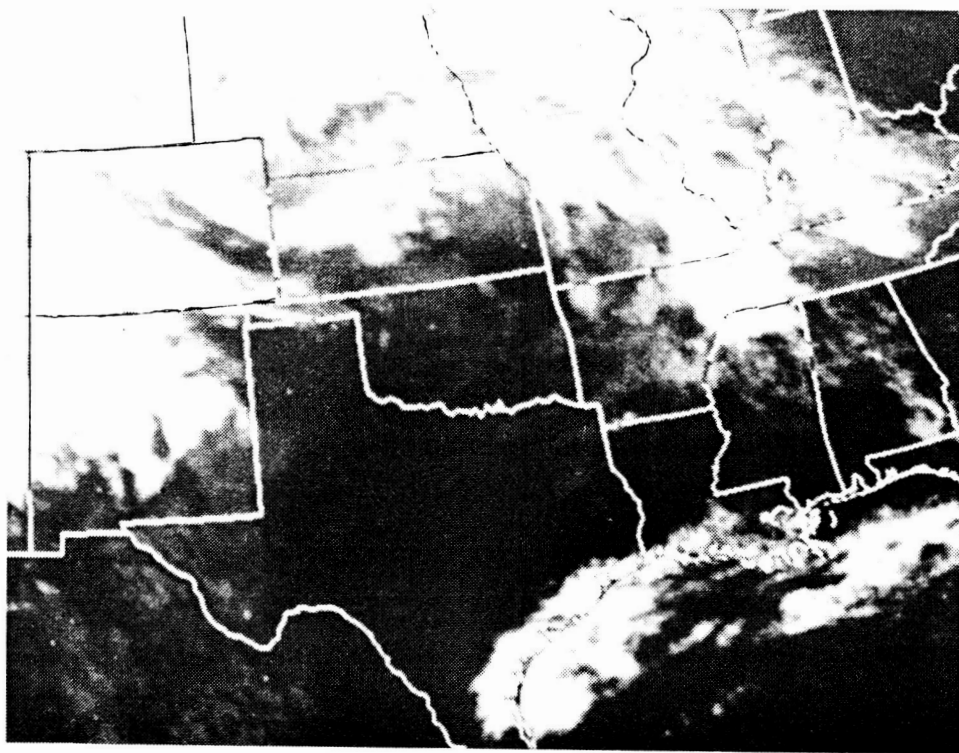


Fig. 4.5. GOES infrared image for 1230Z 10 April 1979.

Colorado, and southwestern Wyoming, of southern Louisiana, and of Indiana and central Kentucky.

The resulting variational result is found in Fig. 4.12. Again, the contour of equal weighting is traced onto the vertical motion field at 450 mb. The weighting function has designated the kinematic method to receive the greater influence in most of the grid. Therefore, the vertical motion patterns at 450 mb are primarily reflections of the kinematic estimate, but with altered magnitudes. Some of the adiabatic vertical velocities, associated with strong thermal advection, have contributed to the vertical motions over Texas to organize a band of rising motion observed to extend from northern New Mexico and bend through the Red River Valley area and well into Louisiana and the Southeastern states. The magnitude over New Mexico has been reduced while the magnitude over west Texas and Louisiana has been slightly increased. At 150 mb, the stability is again large so that nearly total influence is given to the adiabatic estimate. This greatly reduces the magnitude of the vertical velocity in the stratosphere in comparison with the kinematic vertical velocities in Fig. 4.7.

As before, the precipitation echoes from the radar summary of 1735Z are noted on the variational vertical motion field at 450 mb. Some development and intensification has occurred. Main features include a region of thunderstorms with about 16 km cloud tops present over the Red River Valley, and a region of less severe activity in central New Mexico. By 1835Z (not shown), these two systems have merged in a band of precipitation echoes extending across the Texas panhandle and northern Texas. Other precipitation areas of 1735Z are located in

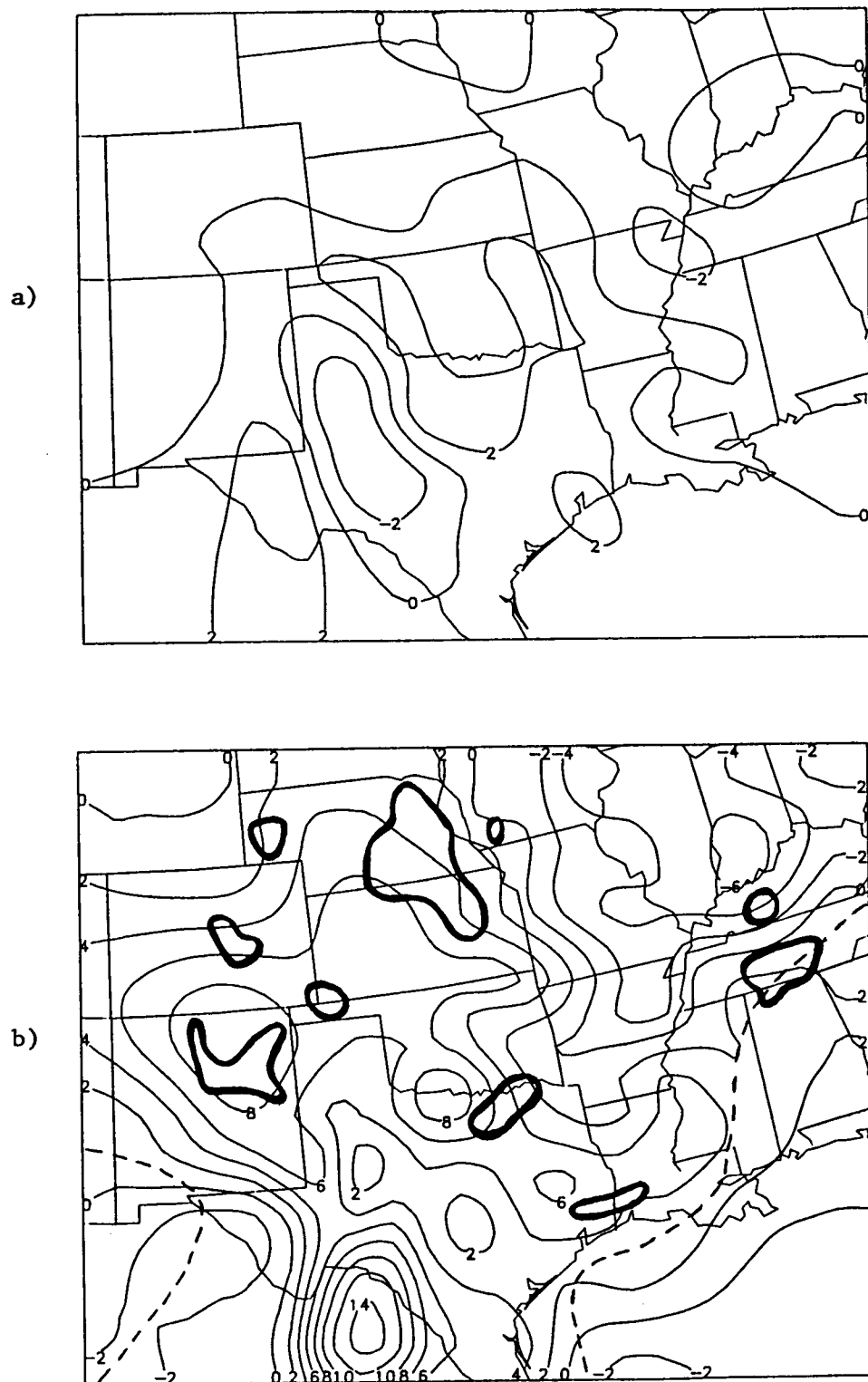


Fig. 4.12. Vertical velocity fields (cm/s) for 18Z 10 April 1979 calculated by the variational algorithm at a) 150 mb and b) 450 mb. In b), bold lines indicate precipitation echoes taken from radar summary and dashed line is $\pi_2 = 10^0$ contour.

Tennessee, Kentucky, eastern Nebraska and Kansas, and southwest Louisiana and southeast Texas.

Still within the period of severe storm activity are the vertical motion fields at 0Z. The kinematic vertical velocity field at 450 mb is shown in Fig. 4.13. It displays a large upward motion region with a maximum greater than 22 cm/s over northern Oklahoma and southern Kansas. Subsidence is found over much of eastern Texas and most of the Midwestern states. At 150 mb, Fig. 4.13a, large magnitudes of vertical velocity exist. The greatest sinking center is over the Red River Valley with a value of about -20 cm/s, and the largest rising center is over northern New Mexico with a value greater than 18 cm/s.

The adiabatic field displayed in Fig. 4.14 shows large centers of alternating sign over Texas, Oklahoma, and Missouri at 450 mb. This is due to strong temperature advection occurring with little or no compensating temperature tendency and also to diabatic processes within the massive area of convective cloudiness over Oklahoma. By 150 mb, weak upward motion is noticed over much of the domain except over central Texas and western Tennessee.

The plot of weighting factor appears in Fig. 4.15. The corresponding contributors to this field are shown in Fig. 4.16. Because much of the northwestern, central, and southwestern areas of the domain could be effected by diabatic processes and because nearly neutral lapse rates exist in eastern Texas, central Colorado and Illinois, the resulting vertical velocity pattern is heavily influenced by the corrected horizontal divergences. The only exceptions are small areas located in southwestern Texas and in northern Alabama and eastern Tennessee. The GOES infrared image in Fig. 4.17 shows a large cloud

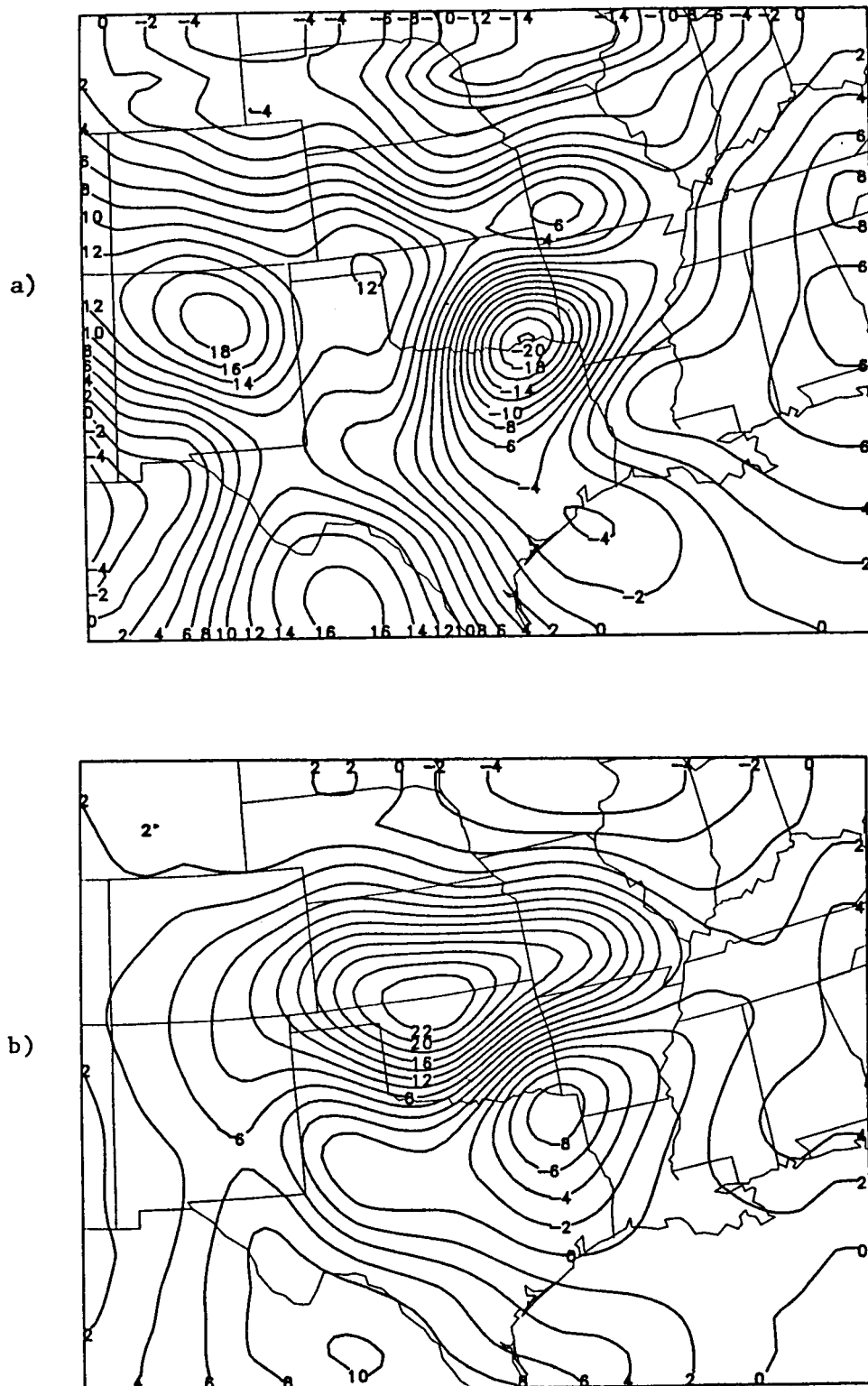


Fig. 4.13. Vertical velocity fields (cm/s) for 0Z 11 April 1979 calculated by the O'Brien adjusted kinematic method at a) 150 mb and b) 450 mb.

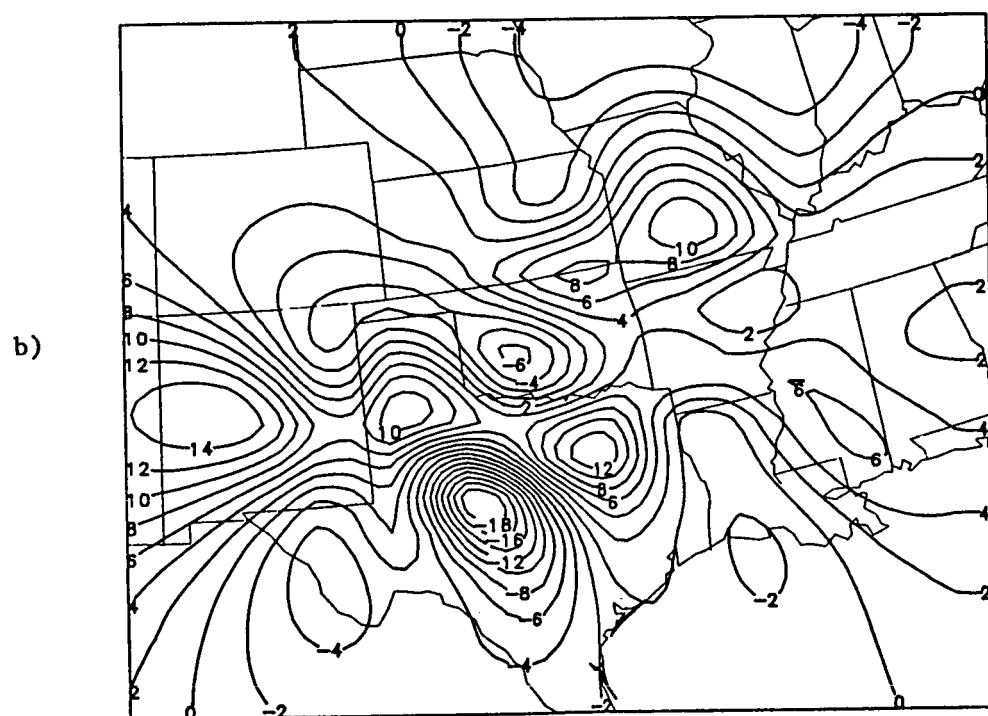
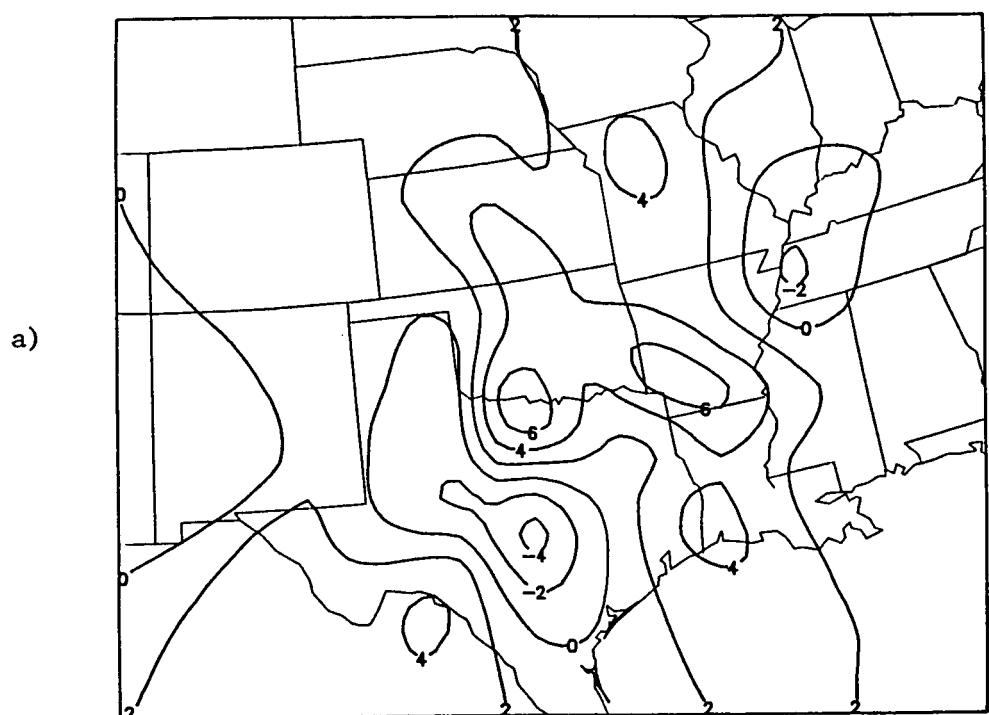


Fig. 4.14. Vertical velocity fields (cm/s) for 0Z 11 April 1979 calculated by the adiabatic method at a) 150 mb and b) 450 mb.

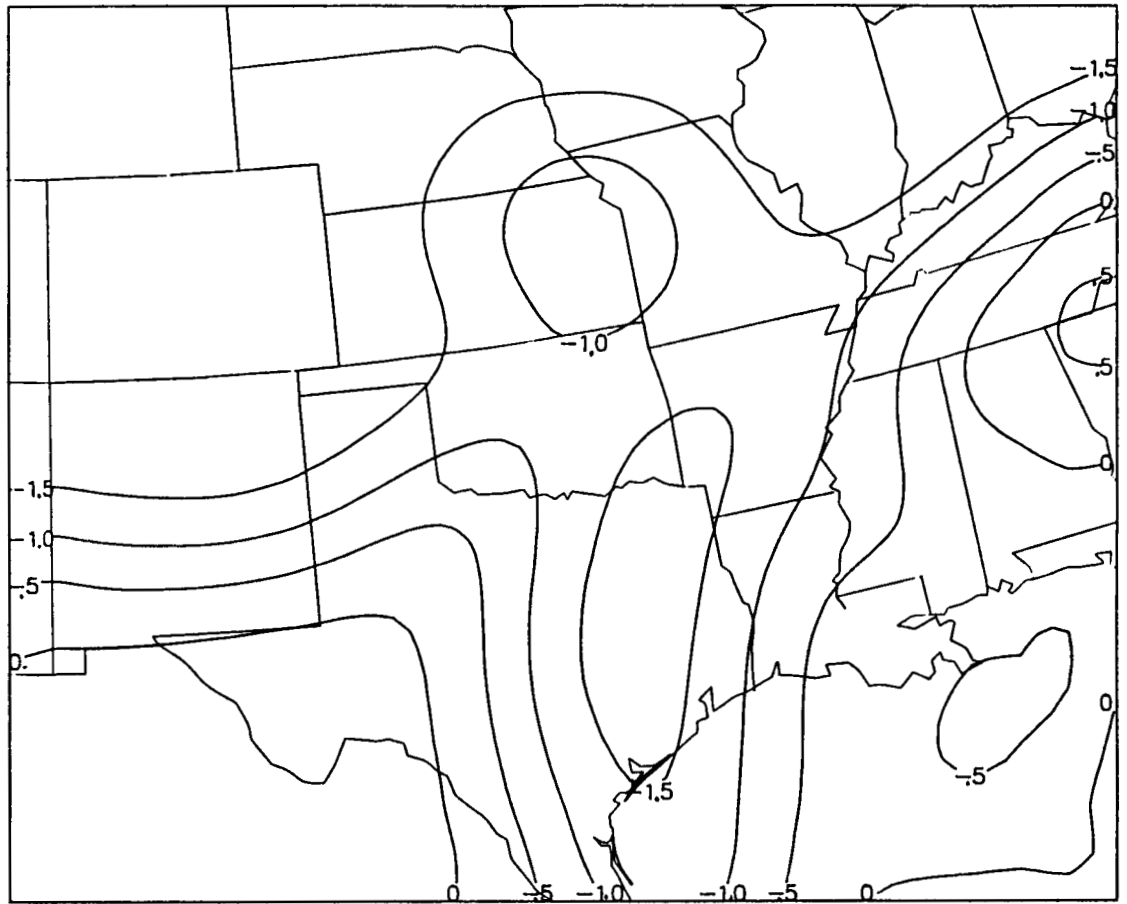


Fig. 4.15. Field of $\log(\pi_2)$ for 0Z 11 April 1979 at 450 mb.

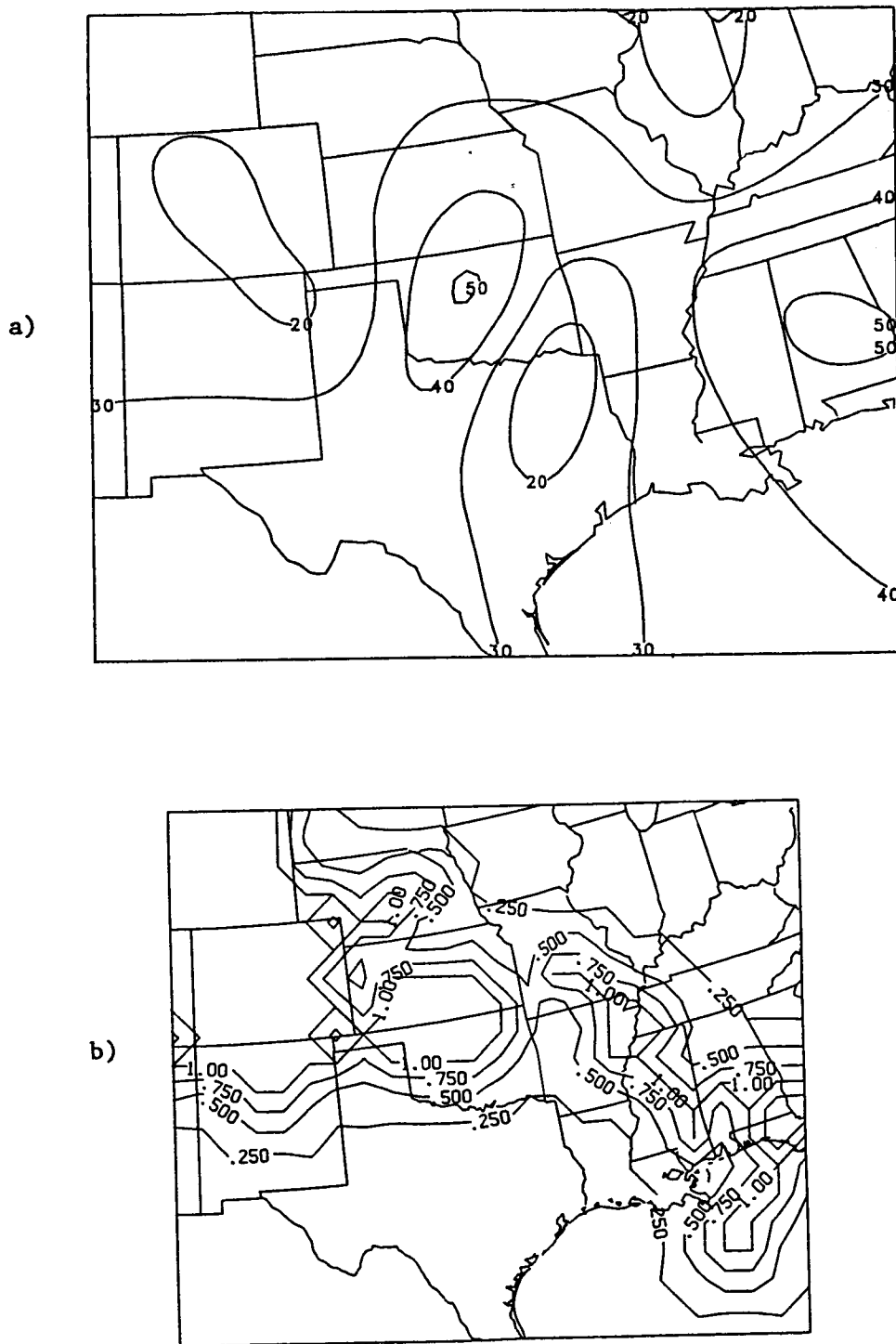


Fig. 4.16. Fields of a) static stability parameter (K/layer) and b) clouds with relative humidity for 0Z 11 April 1979 at 450 mb.

ORIGINAL PAGE IS
OF POOR QUALITY

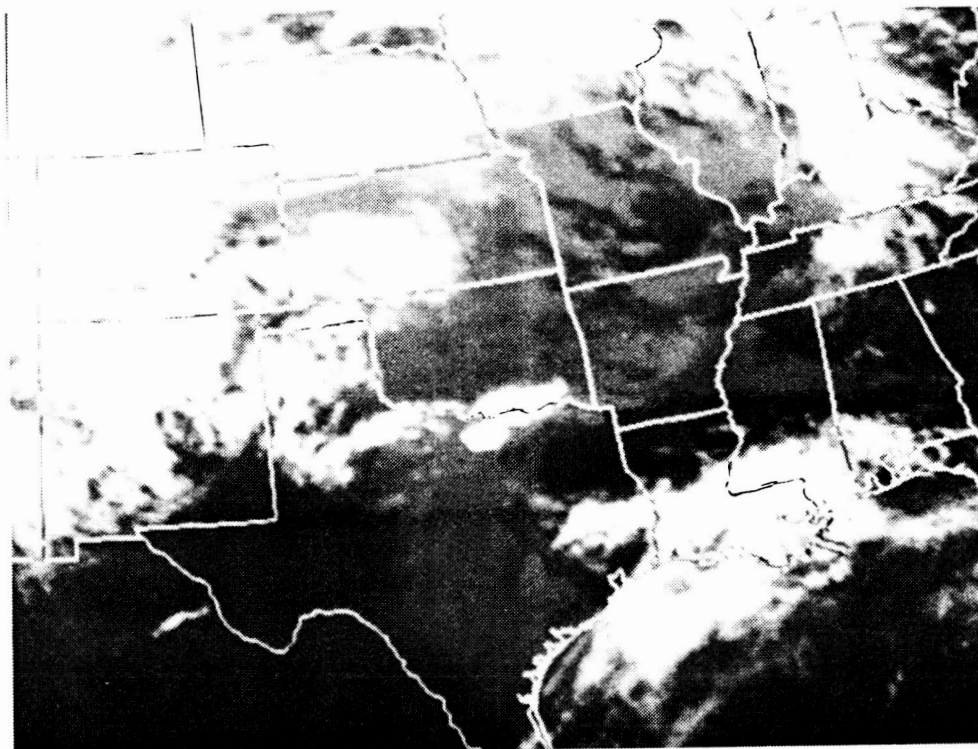


Fig. 4.11. GOES infrared image for 1800Z 10 April 1979.

mass present over much of Oklahoma and Kansas. The relative humidity indicates that sufficient moisture exists at 450 mb for only the northern portion of the cloud mass. This may occur because the resolution of the relative humidity data may not be fine enough to detect moisture over the Red River Valley where strong thunderstorms are known to be present at this time.

Shown in Fig. 4.18 are the variational fields for 0Z. Again, at 450 mb, the contour depicting nearly equal weight of the two methods is traced on the field. Since this time period is dominated by deep cloudiness and moist conditions, the kinematic estimate tends to control the variational result at this level. One major feature that the adiabatic estimate contributed is the increased magnitude of sinking motion over central Texas. The adiabatic estimate receives greater weight than the horizontal divergence at 150 mb. This is still due to the very stable conditions at this layer.

By 6Z, most of the severe weather had diminished. The kinematic estimate, in Fig. 4.19, shows an intense band of rising motion at 450 mb. This band extends over central Texas, central Oklahoma, Missouri, and Kansas. At 150 mb, very strong centers with magnitudes greater than 34 cm/s are present.

Presented in Fig. 4.20 are the adiabatic vertical velocity estimates for 6Z. The adiabatic field at 450 mb has large centers with alternating sign similar to the 0Z field. Again, this results from strong temperature advection with little compensating temperature tendency and may also be associated with strong diabatic processes at the tops of strong thunderstorms over Texas and Oklahoma. At 150 mb, much of Texas is experiencing downward motion, and over southwestern

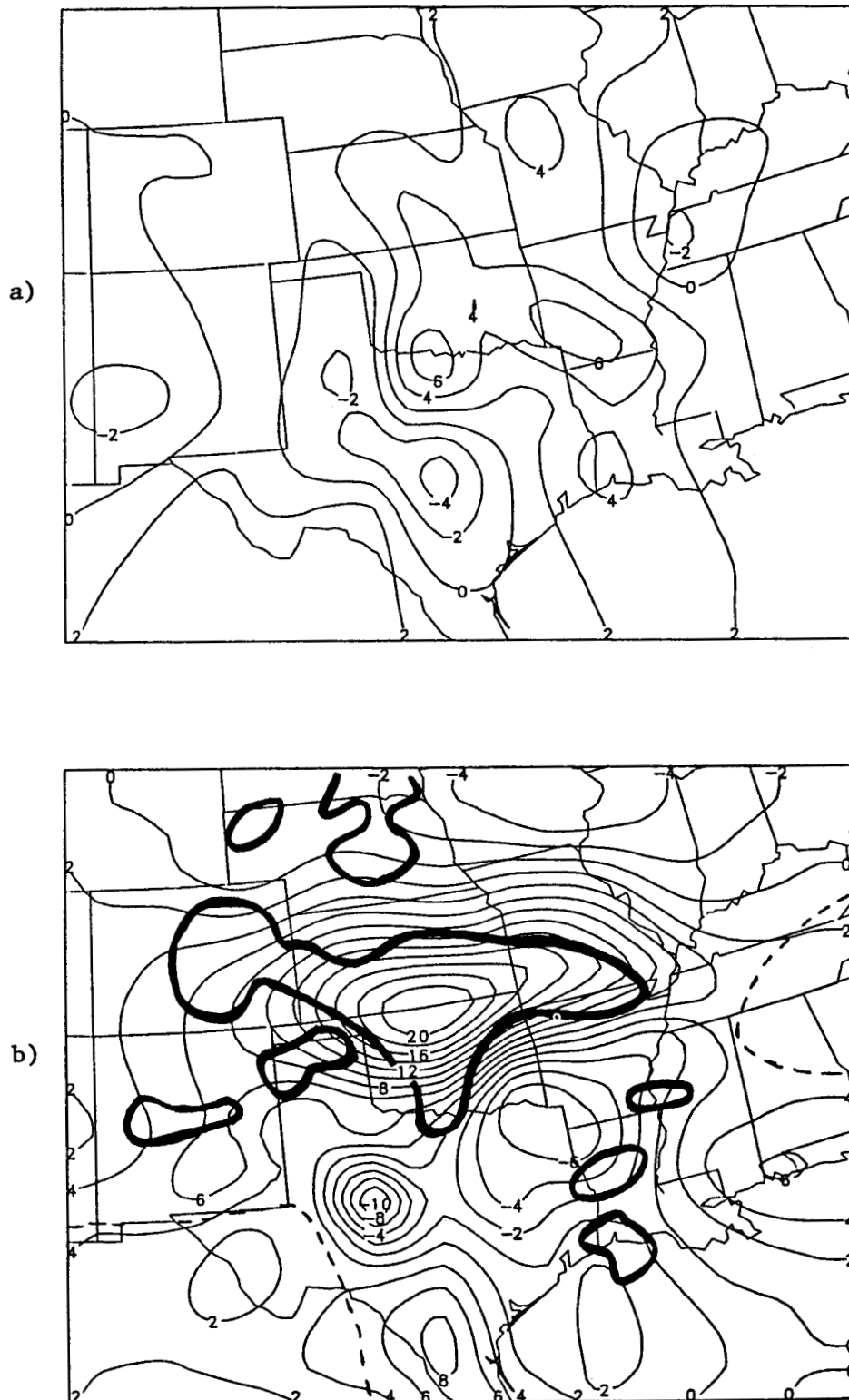


Fig. 4.18. Vertical velocity fields (cm/s) for 0Z 11 April 1979 calculated by the variational algorithm at a) 150 mb and b) 450 mb. In b), bold lines indicate precipitation echoes taken from radar summary and dashed line is $\pi_2 = 10^0$ contour.

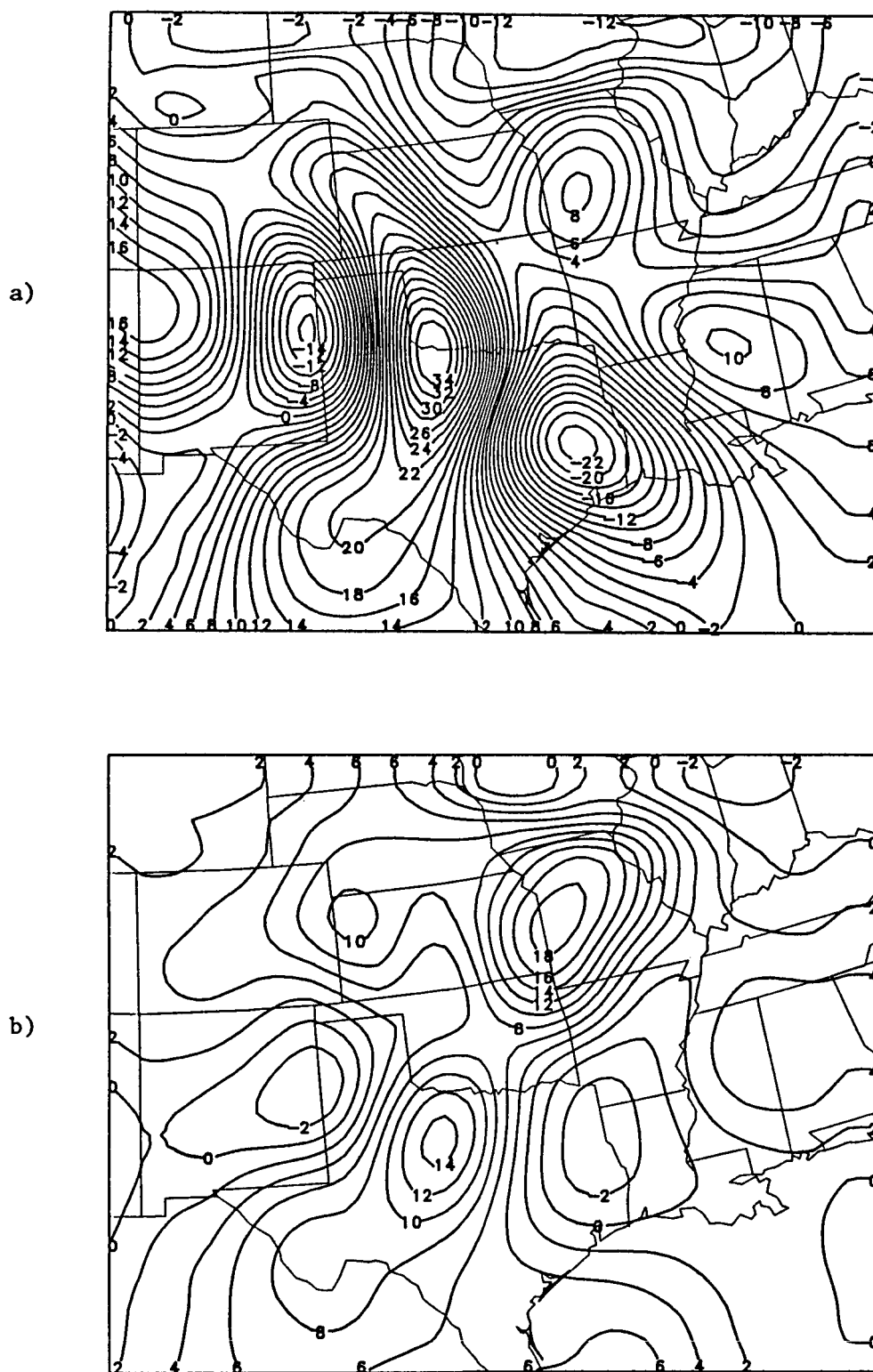


Fig. 4.19. Vertical velocity fields (cm/s) for 6Z 11 April 1979 calculated by the O'Brien adjusted kinematic method at a) 150 mb and b) 450 mb.

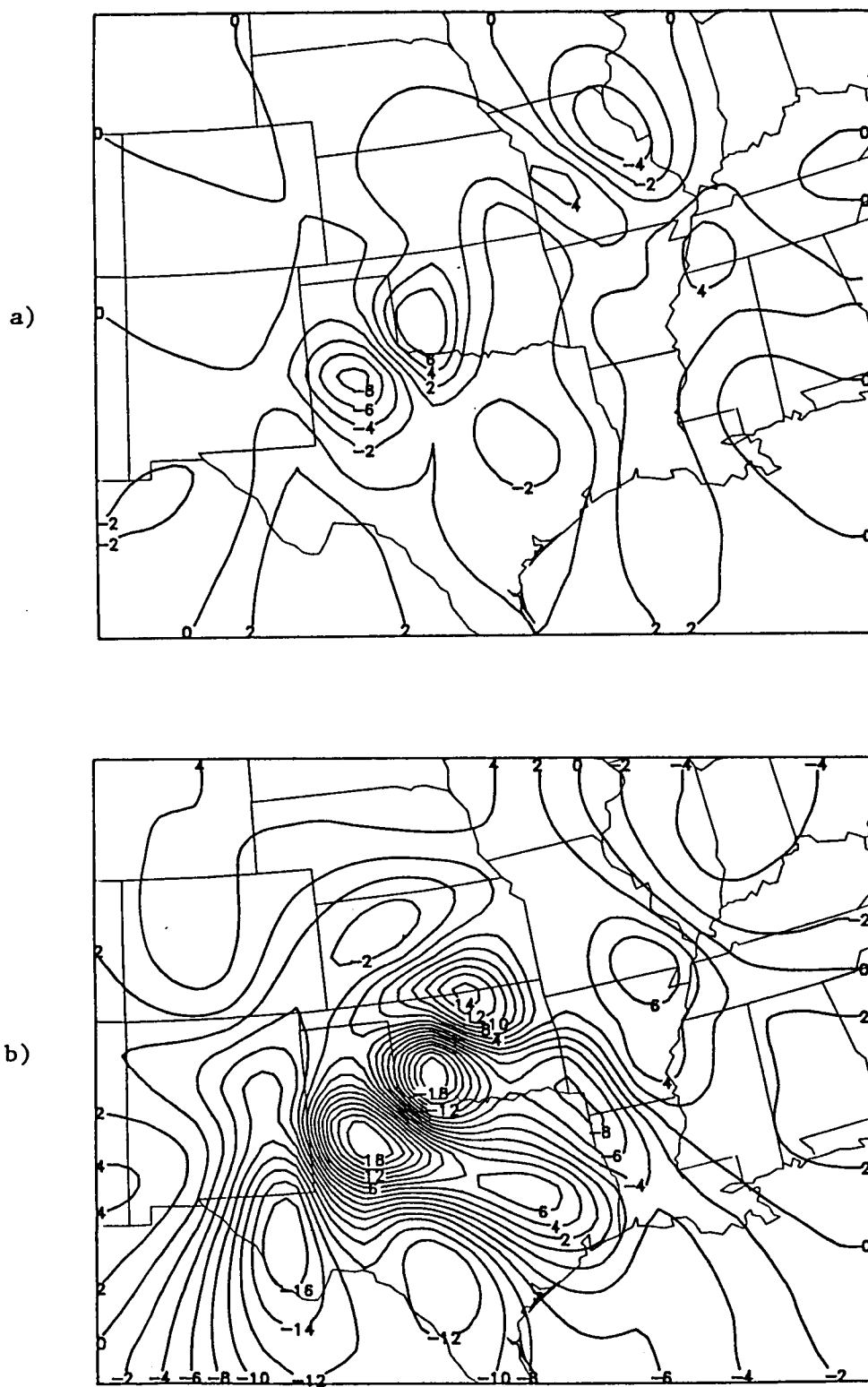


Fig. 4.20. Vertical velocity fields (cm/s) for 6Z 11 April 1979 calculated by the adiabatic method at a) 150 mb and b) 450 mb.

Oklahoma and northern Mississippi centers of rising motion exist. However, due to the increased stability of the lower stratosphere, these velocities are much smaller than the velocities obtained from the O'Brien kinematic method.

A plot of the weighting factor, π_2 , is displayed in Fig. 4.21. Fields of the horizontally varying, contributing factors appear in Fig. 4.22. Stability parameter shows only a small region of near neutral lapse rates over southwestern Texas. The cloudiness with relative humidity exhibits that nearly the entire northern half of the grid may be experiencing diabatic heating or cooling. The GOES infrared image in Fig. 4.23 shows an elongated cloud feature, but the relative humidity supports only the northern portion of this feature at 450 mb. This is perhaps caused by the coarse resolution of the relative humidity data which cannot detect moist regions of scale smaller than the station spacing.

Because of the cloudiness and moisture, the variational field at 450 mb, shown in Fig. 4.24, is controlled primarily by the kinematic estimate. The band of upward motion is still present, but with altered magnitudes. As usual at 150 mb, Fig. 4.24a, the adiabatic estimate increases its contribution and dominates the variational result.

Precipitation echoes from the 0535Z radar summary are traced on the 450 mb variational result. A large region of precipitation is still present, but the intensity of the system is decaying.

B. Vertical Velocity Results: Vertical Profiles

Several vertical velocity profiles were developed for the entire case period. These profiles describe the structure of the vertical wind

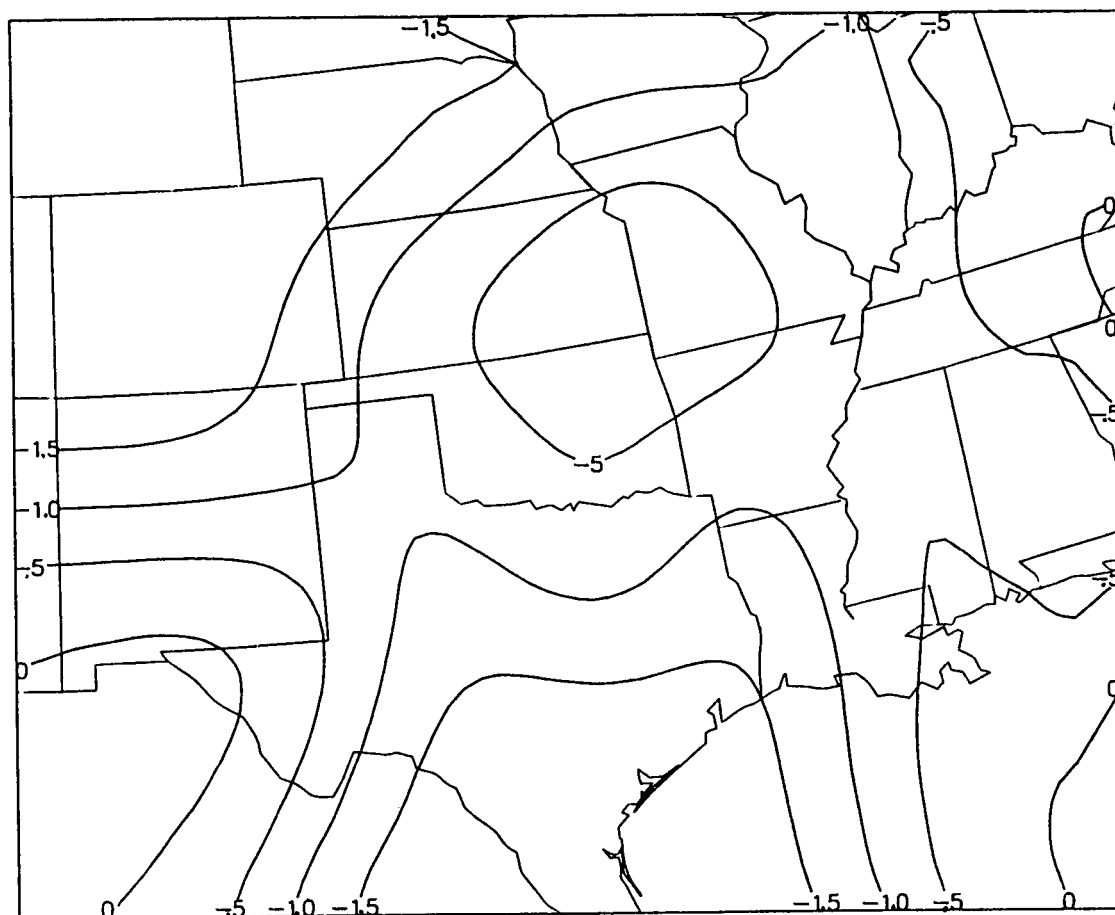


Fig. 4.21. Field of $\log(\pi_2)$ for 6Z 11 April 1979 at 450 mb.

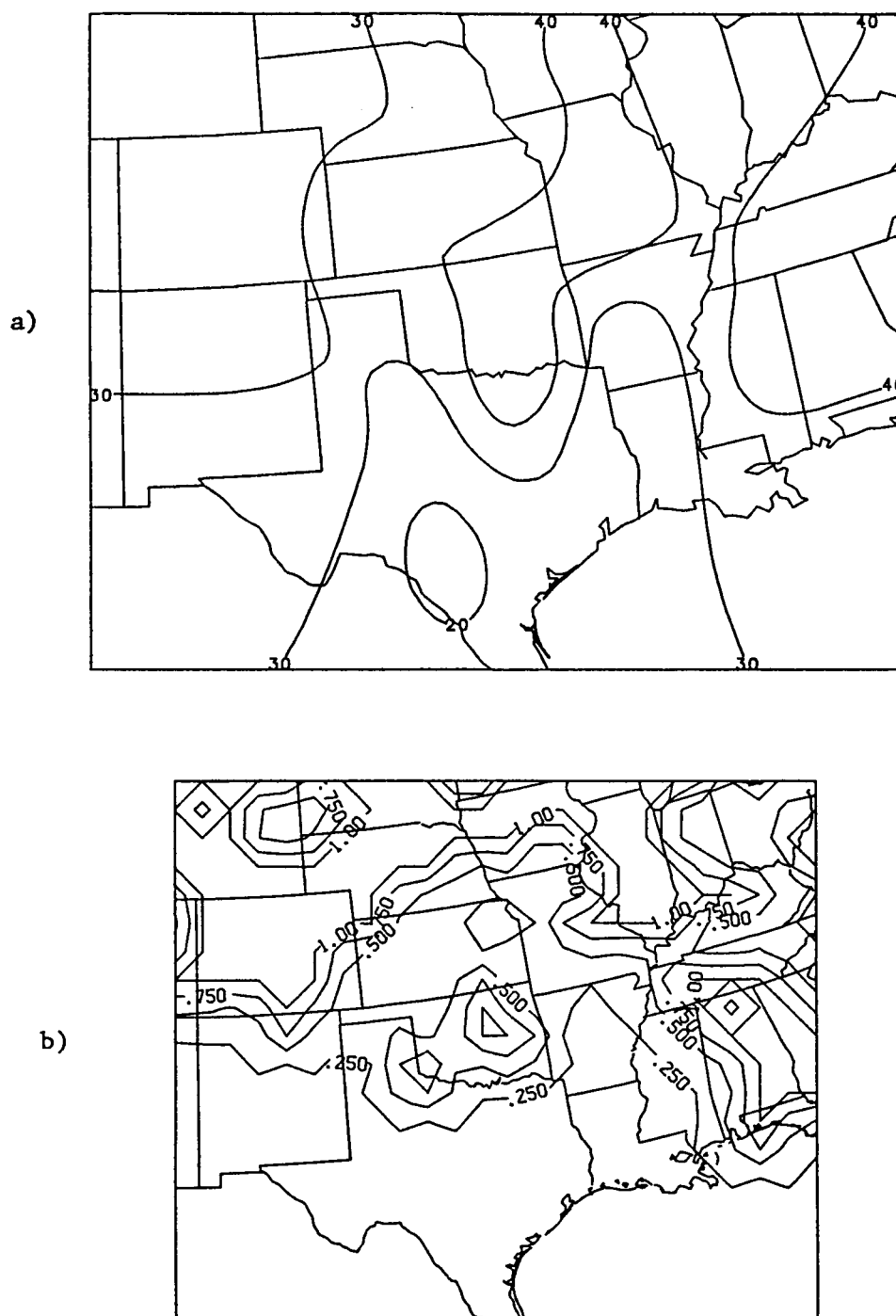


Fig. 4.22. Fields of a) static stability parameter (K/layer) and b) clouds with relative humidity for 6Z 11 April 1979 at 450 mb.

ORIGINAL PAGE IS
OF POOR QUALITY

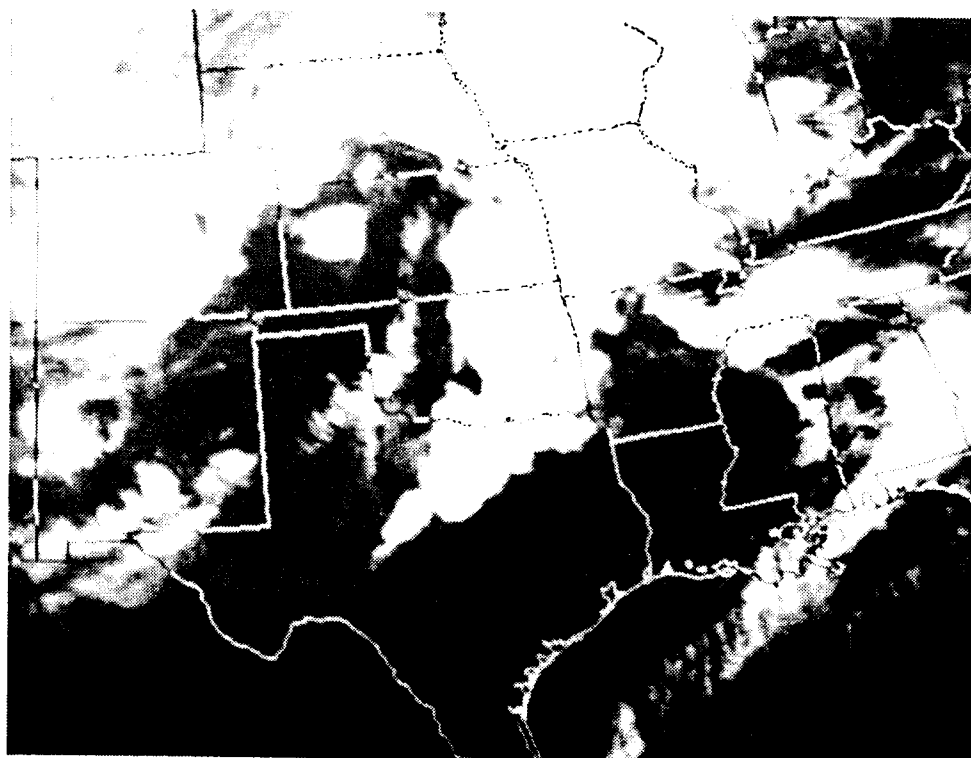


Fig. 4.23. GOES infrared image for 0600Z 11 April 1979.

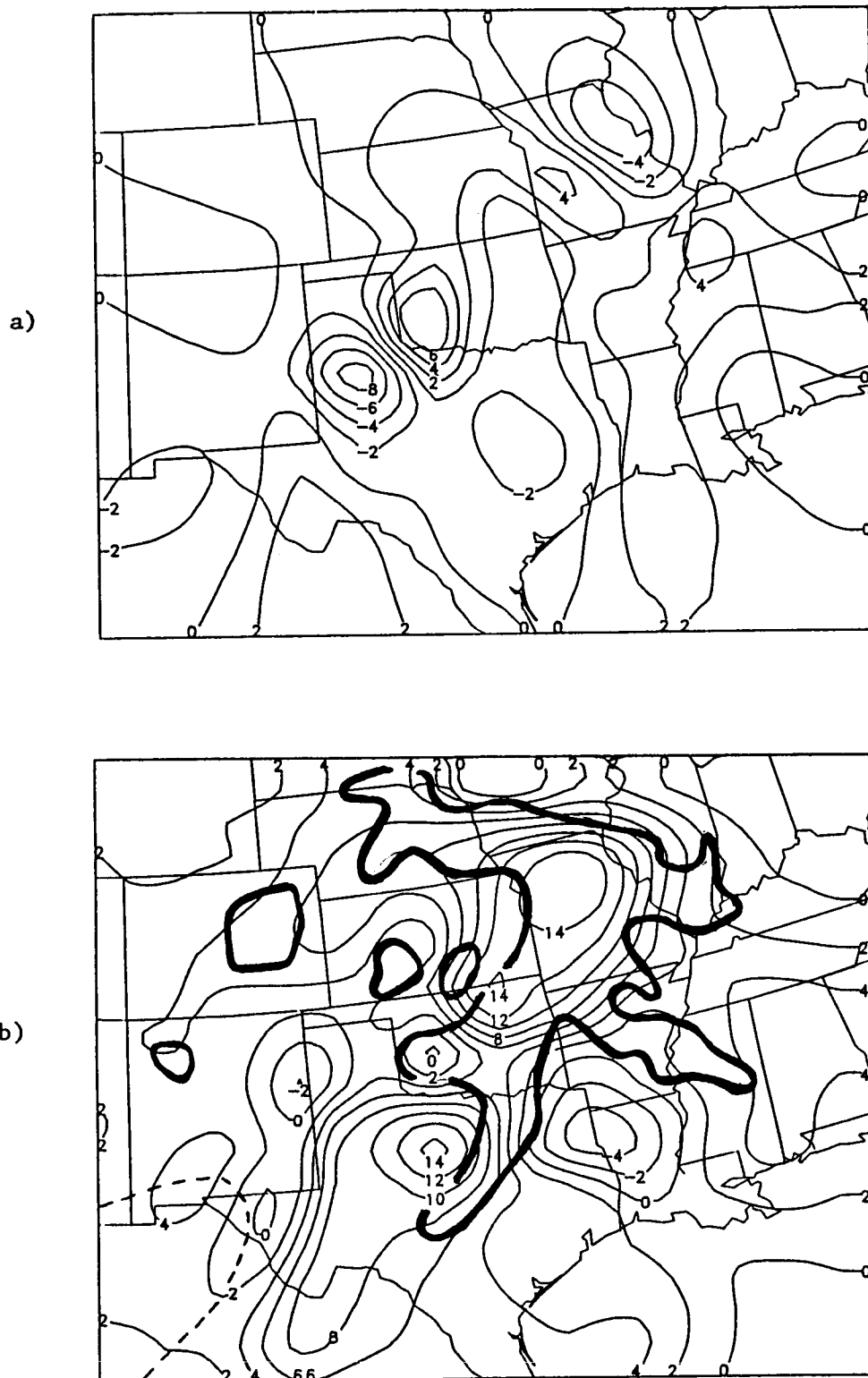


Fig. 4.24. Vertical velocity fields (cm/s) for 6Z 11 April 1979 calculated by the variational algorithm at a) 150 mb and b) 450 mb. In b), bold lines indicate precipitation echoes taken from radar summary and dashed line is $\pi_2 = 10^0$ contour.

component with respect to the vertical coordinate. The profiles of the three methods, O'Brien kinematic, adiabatic, and variational, are placed on the same plot so that they may be easily compared. Adjacent to the vertical velocity profile is the profile for the logarithm of the weighting function. Negative values reveal that the O'Brien corrected horizontal divergences are receiving more weight, and positive values show that the adiabatic estimate is accorded stronger influence. Four representative vertical velocity profiles are displayed in Figs. 4.25, 4.26, 4.27, and 4.28. The locations of the profiles are indicated on the domain in Fig. 3.1. These are selected because they exhibit both the pre-storm and storm environments, and because they provide observations that were not obvious from the horizontal fields alone.

The first two profiles are for 12Z 10 April. The profile in Fig. 4.25 is located in northern Kansas. At this time and location, light precipitation and cold cloud tops exist as was demonstrated in Figs. 4.5 and 4.6. This plot shows that the adiabatic and kinematic methods produce comparable estimates of vertical velocity up to level 2 (about 850 mb). The results of the two methods then depart in the upper levels, varying not only in magnitude, but also in sign. The variational result achieves a reasonable compromise between the two methods, and above level 8 (250 mb) it closely follows the adiabatic estimate. The latter avoids the unrealistically large kinematic estimates within the highly stable stratosphere. The profile of weighting function shows that the variational result agrees with the amount of influence accorded to each method.

The profile for the same time, but located in central Missouri, is found in Fig. 4.26. Again, light precipitation and cold cloud top

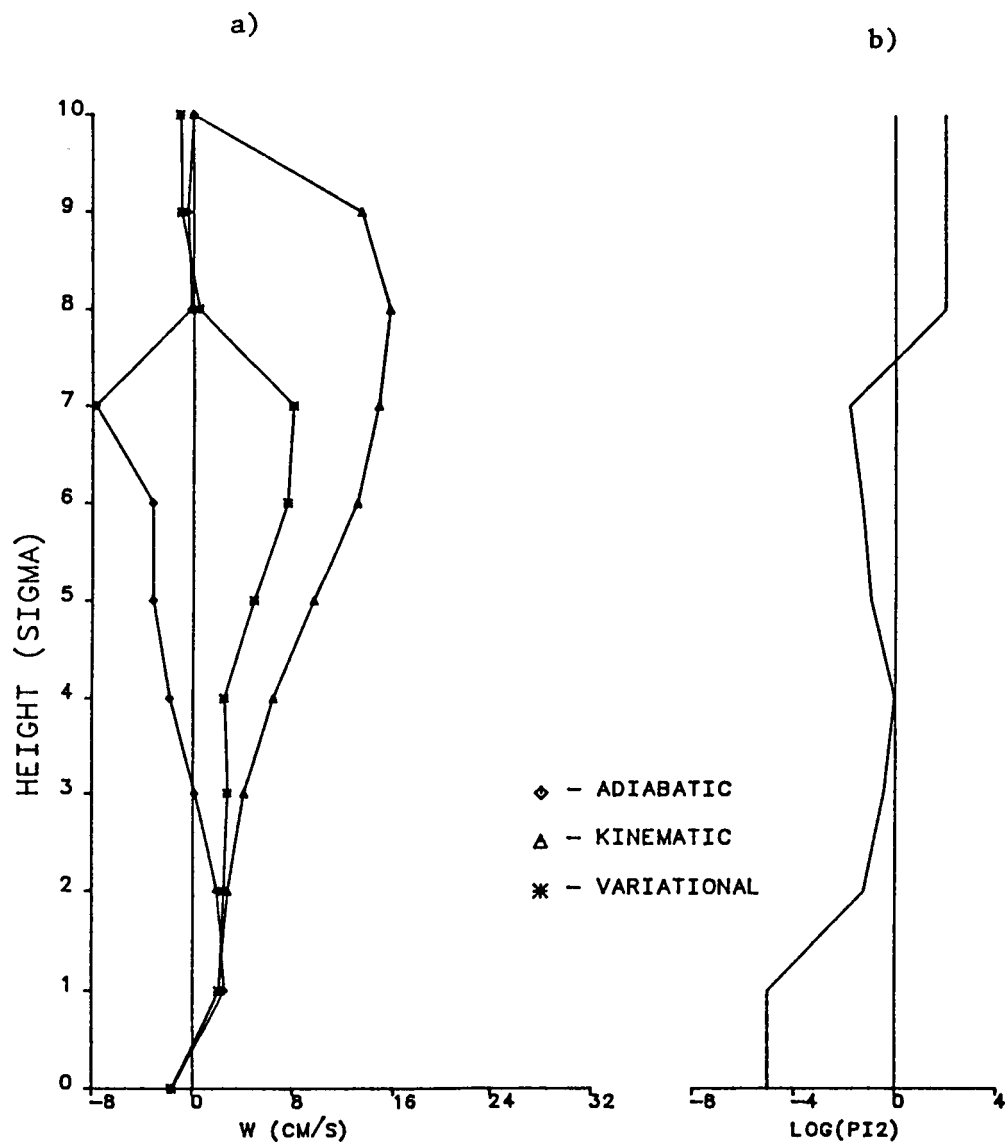


Fig. 4.25. Vertical profiles of a) vertical motion (cm/s) and b) $\log(\pi_2)$ at northern Kansas for 12Z 10 April 1979.

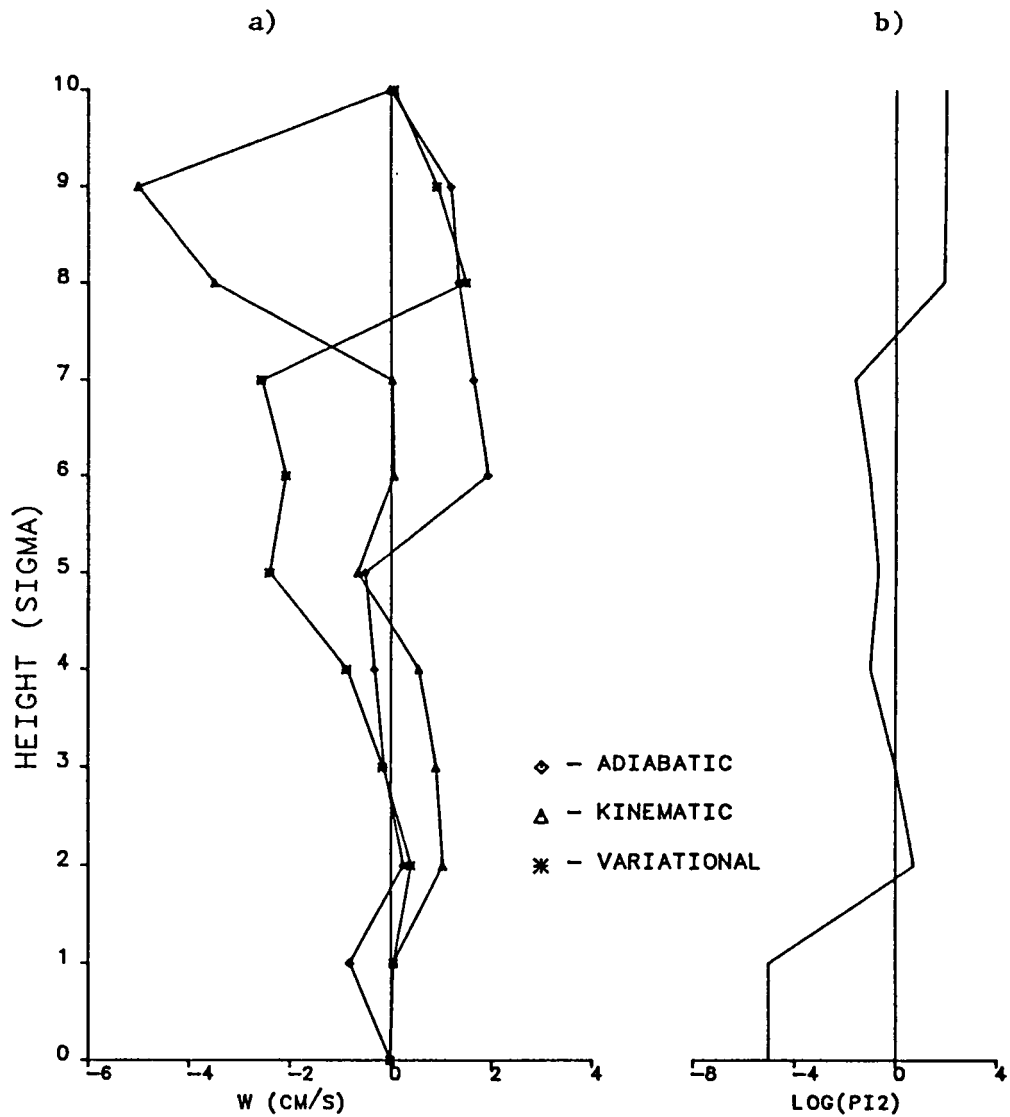


Fig. 4.26. Vertical profiles of a) vertical motion (cm/s) and b) $\log(\pi_2)$ at central Missouri for 12Z 10 April 1979.

temperatures were evidenced for this location in Figs. 4.5 and 4.6. Except for levels 8 and 9 (250 mb and 150 mb, respectively), the kinematic and adiabatic estimates are not drastically different as seen in the aforementioned profile. From the profile of weighting function, though, it can be observed that at levels 5 through 7 (550 mb through 350 mb) that the variational result did not ideally respond to the weights. Instead, the variational vertical velocity over-corrected for the divergence magnitude resulting in about a -3 cm/s value at level 7. Here the adiabatic estimate suggests upward motion, where corrected kinematic divergence, represented by the slope of the O'Brien kinematic profile, demonstrates no change in vertical motion for that layer. This discrepancy may be a response of a three-dimensional coupling of the algorithm allowing information from surrounding grid points to influence the result.

The third profile, Fig.4.27, is constructed for 18Z 10 April at western Missouri. For this time and location, no precipitation echoes or cold cloud top temperatures were found from Figs. 4.11 or 4.12. Between levels 4 and 8 (650 mb and 250 mb, respectively), the kinematic and adiabatic estimates produce very different vertical velocity profiles. The response of the variational algorithm is to develop velocity values which oscillate around 0 cm/s. Below level 4, the variational result closely parallels the kinematic profile even though the weighting function at level 2 (850 mb) is dictating more strength to the adiabatic estimate. This again may be caused from information of surrounding grid points being transferred into the result. Levels 8 and above largely have influence from the adiabatic method producing small magnitudes of vertical motion. This is a desirable result since small

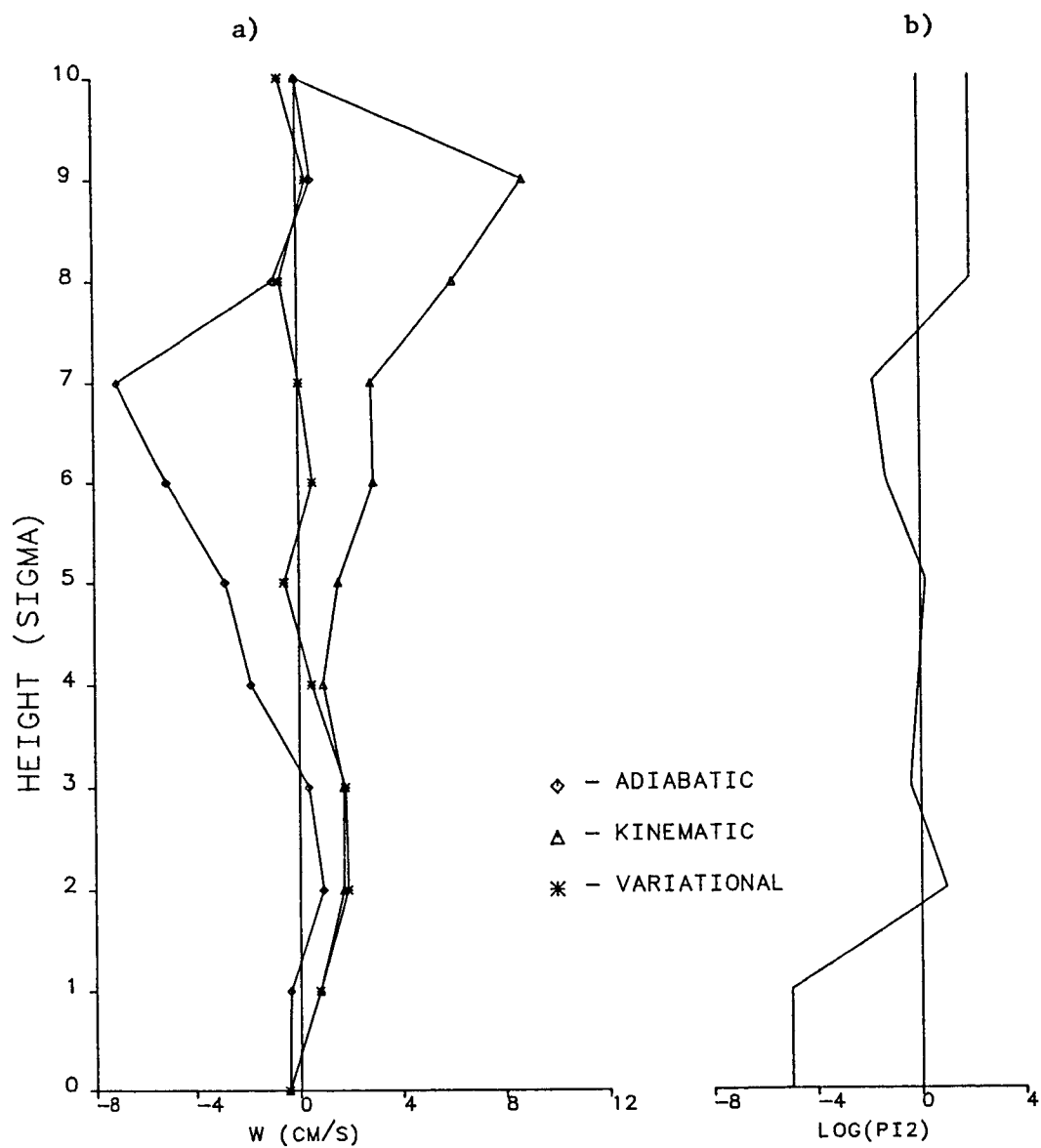


Fig. 4.27. Vertical profiles of a) vertical motion (cm/s) and b) $\log(\pi_2)$ at western Missouri for 18Z 10 April 1979.

vertical velocities should be expected in the highly stable stratosphere.

In Fig. 4.28 is the profile for 0Z 11 April at northern Oklahoma. At this time and location, a large, deep cloud mass is present as seen from the GOES infrared image (Fig. 4.17). Since diabatic processes are likely here, the kinematic method is considered more physically acceptable. This is reflected in the profile of weighting function because nearly entire weight is given to the O'Brien corrected divergence except for levels 8 (250 mb) and above which give primary weight to the adiabatic estimate. Consequently, The variational result parallels the kinematic result with only a slight reduction of magnitude. Levels 8 and above reproduce the adiabatic profile almost exactly. Even with this reasonable result, it can be seen that levels 2 and 3 (850 mb and 750 mb, respectively) have had some outside influence. This is probably again due to surrounding information creeping into the final solution.

Observations of the vertical profiles prompted further investigation of the theory which revealed that even though the approach used for this work is correct, other forms of the solution might prove to yield more favorable results.

For this study, Eq. 2.13 was used to solve for vertical motion with a horizontally varying function describing π_2 . The vertical motion could not be restored by the adjustment because the solution of the Lagrange multiplier produced a slightly smoothed adjustment field. Also, the solution of λ involved division by π_2 . When the value of π_2 became quite small, the result became unreasonably large, where had been smoothed across the sharp gradients of π_2 . It was for this

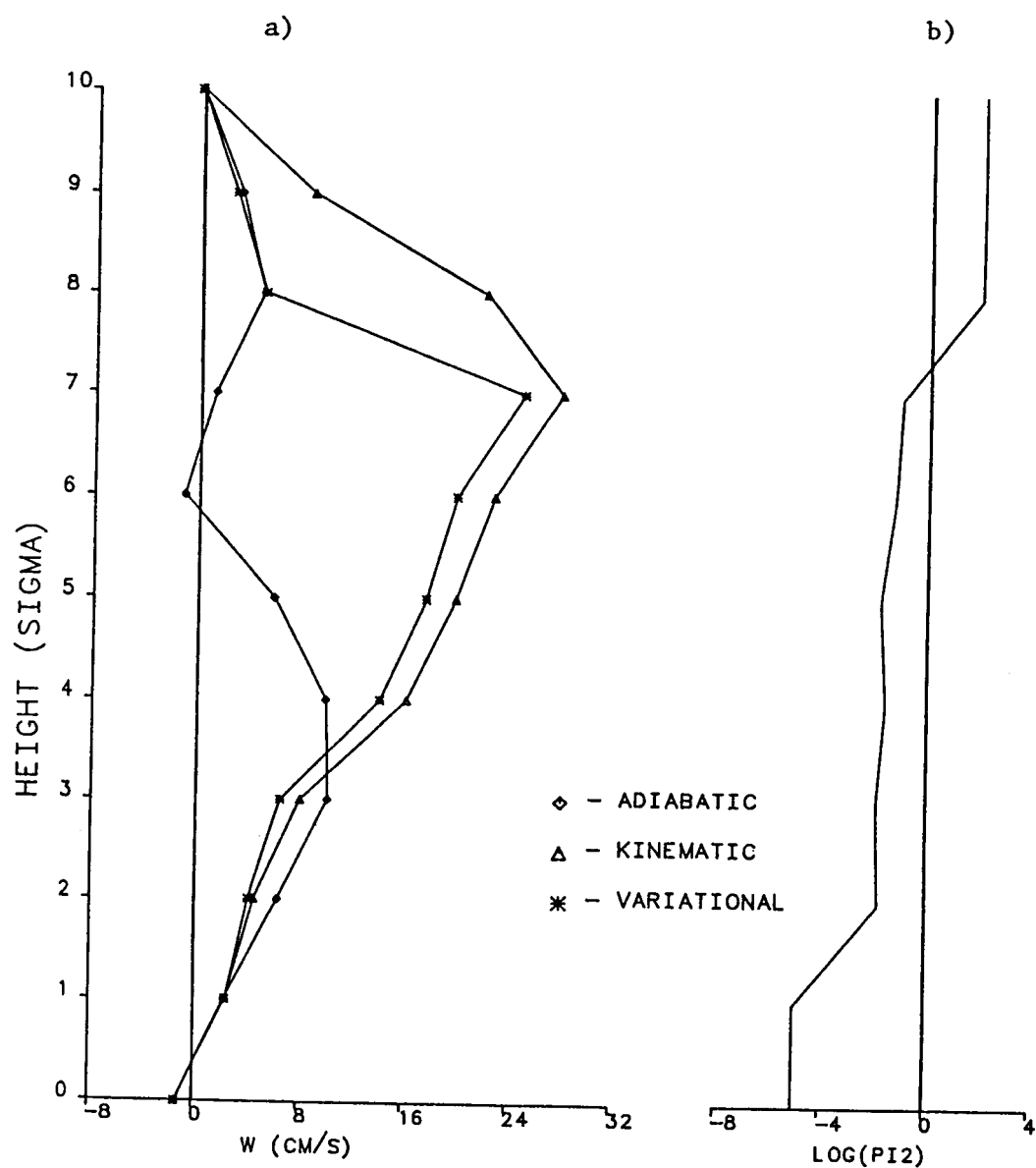


Fig. 4.28. Vertical profiles of a) vertical motion (cm/s) and b) $\log(\pi_2)$ at northern Oklahoma for 0Z 11 April 1979.

reason that the weighting function was smoothed before incorporating it into the algorithm.

Another method tried, but not presented here, was to use Eq. 2.16 to solve for the vertical velocity. Problems occurred when π_2 became very small and the adjustment term dominated the solution. To alleviate this, π_2 was normalized so that all horizontal variation was transferred to π_1 . This caused additional difficulty since a large value of horizontal gradient in π_1 violated stability criteria when solving for the Lagrange multiplier. It was determined that π_1 could vary by four orders of magnitude per grid space without violating criteria. Another unfortunate result was that the solution of the Lagrange multiplier smoothed the adjustment field according to the magnitude of the forcing function, Eq. 2.20. This could allow the vertical velocity solution to be influenced by neighboring points.

CHAPTER V

DISCUSSION

A vertical velocity algorithm was developed which blended the kinematic and adiabatic methods. Since the two techniques possess complimentary strength and weaknesses, it was desirable to combine the methods such that the strengths of each method were built into the algorithm and the weaknesses were minimized. This blending was accomplished by the use of numerical variational analysis. This algorithm was tested using the AVE-SESAME I data set.

Two constituents which determined the variational results were the divergences of the adjusted horizontal wind which when vertically integrated yield the O'Brien kinematic vertical velocity and the adiabatic estimate of vertical motion. To assign the contribution of each quantity, a weighting function was constructed. Criteria were determined so that more influence was given to that factor which better agreed with physical processes. Specifically, O'Brien kinematic divergence values were given greater influence in regions of diabatic heating and of near neutral stability. Conversely, the adiabatic value received stronger influence in clear or stable regions.

Results showed that the variational result in most cases succeeded in finding a compromise between the two techniques. A triumph of the variational algorithm was permitting the adiabatic method to dominate near or above the tropopause. Since this lower stratospheric region is very stable, near zero values of vertical velocity are expected. The weighting function responded to the large values of static stability parameter in this layer and caused the adiabatic estimates to have

primary weight in the variational solution. This is a desirable result since, in this layer, O'Brien corrected kinematic values are typically much larger than the adiabatic values. Hence, the variational algorithm has allowed a thermodynamic property of the atmosphere, static stability, to determine a more reasonable vertical velocity estimate.

Some problems were encountered in solving for the variational vertical motion estimate. These are of both a meteorological and a numerical nature.

A meteorological difficulty is that the resolution of the rawinsonde relative humidity soundings is very coarse. Therefore, the moisture criteria of the weighting function may suffer if small-scale features, such as cumulonimbus towers penetrating a dry layer, cannot be detected. This leads to a further difficulty. The adiabatic method produces a "point" estimate of vertical motion, while the kinematic method yields an area-averaged value. Again, if small-scale convection is not resolved, the two methods can produce estimates of differing magnitude and sign. Therefore, in areas where small-scale convection is suspected, further data may be required to provide a reasonable variational result.

In some cases, the variational algorithm appeared to either over-correct the final vertical velocity or to not allow the appropriate method to control the result. This is a numerical problem which may be due to information from surrounding grid points being transferred into the variation solution.

Other numerical problems concern the weighting function. With some additional investigation, it was discovered that sharp gradients and certain magnitudes of the weighting function could provide some

undesireable results in the adjustment field. Attempts to correct these difficulties have not yet yielded satisfactory results.

In conclusion, the variational vertical velocity algorithm has combined two commonly used techniques, the kinematic and adiabatic methods. This algorithm attempts to blend the strengths of these methods, while minimizing their weaknesses. Since vertical velocities are not easily or reliably measured, "ground truth" of this quantity is unknown. In most cases the algorithm produced vertical motion fields which were reasonable with regard to prevailing weather conditions.

APPENDIX A

EXAMPLE OF DIVERGENCE CALCULATION FOR ANALYTIC FIELD

As mentioned by Chien and Smith (1973) and Goodin et al (1979) the kinematic method is very sensitive to the scheme chosen to approximate the horizontal divergence field. Belt and Fuelberg (1982) introduced random error into a mesoscale data set prior to computations of kinematic quantities. Their results revealed that the divergence field suffered greatest from these random errors.

To demonstrate that spurious divergence values are introduced by numerical procedures, a non-divergent, analytic stream function is employed. This non-dimensionalized function is described on a Cartesian grid by

$$\psi = By + Ae^{-\alpha} \quad (\text{A.1})$$

where

$$\alpha = a(x-x_0)^2 + b(y-y_0)^2$$

The quantities A, B, a, and b are constants, and x_0 and y_0 are the coordinates of the center of the grid. This stream function is presented in Fig. A.1

The u- and v-components of horizontal velocity are determined from differentiating the stream function. These expressions for a Cartesian grid are

$$u = -\partial\psi/\partial y = -B + 2bA(y-y_0)e^{-\alpha} \quad (\text{A.2})$$

$$v = \partial\psi/\partial x = -2aA(x-x_0)e^{-\alpha} \quad (\text{A.3})$$

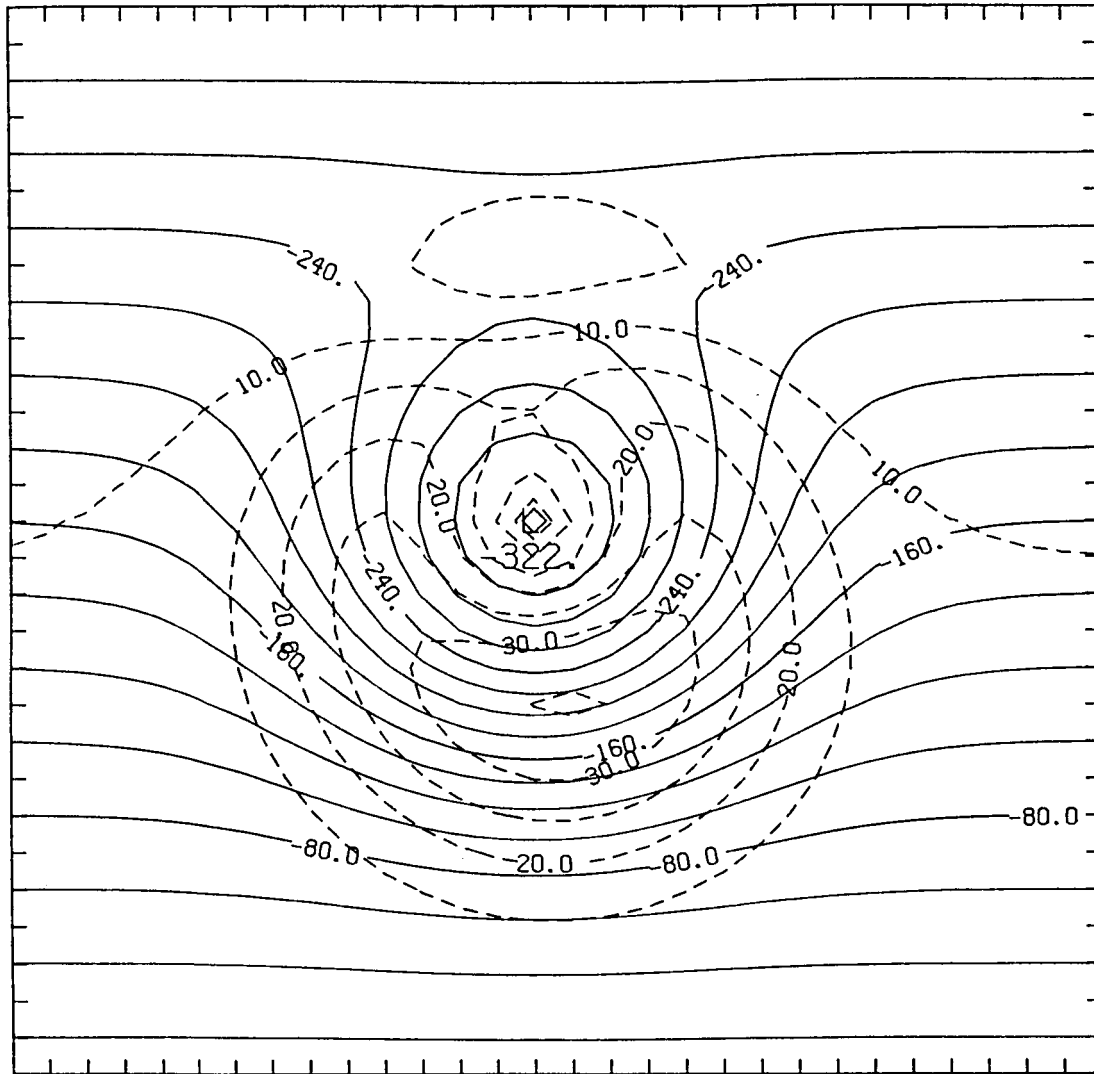


Fig. A.1. Plot of non-divergent, analytic stream function (solid lines). Dashed lines are corresponding isotachs. All values are non-dimensionalized.

For the work presented here, a square grid is chosen to be thirty grid space units (gsu) on each side. The values for the constants are selected as follows in Table A.1.

A	B	a	b	x_0	y_0
-166.7	-10.0	0.03125	0.03125	15	15

Table A.1. Non-dimensionalized constants for analytic stream function.

These constants are selected such that the disturbance in the ψ field appears in the center of the grid and has a half-wavelength of about ten gsu. Also, the extrema in the v field are positioned at four gsu from either side of the origin and have a magnitude of about 25. Lastly, the u values approach 10 infinitely far from the origin.

Divergence of the horizontal velocity field is approximated by using a second-order, finite difference scheme on a staggered grid. This grid is shown in Fig. A.2. Since the given analytic field is non-divergent, the values calculated with the finite difference scheme are actually the truncation error of the scheme. If this non-zero value of divergence is assumed to exist throughout a layer in the atmosphere, then from the conservation of mass principle, a corresponding vertical component of motion must be present. Hence, erroneous values of vertical motion can be introduced from the use of a finite difference scheme to calculate divergence.

The result of objectively analyzing ψ , u , and v fields with a variation of the Barnes (1973) scheme is demonstrated. This scheme is used to objectively analyze observations onto a 30 gsu by 30 gsu grid.

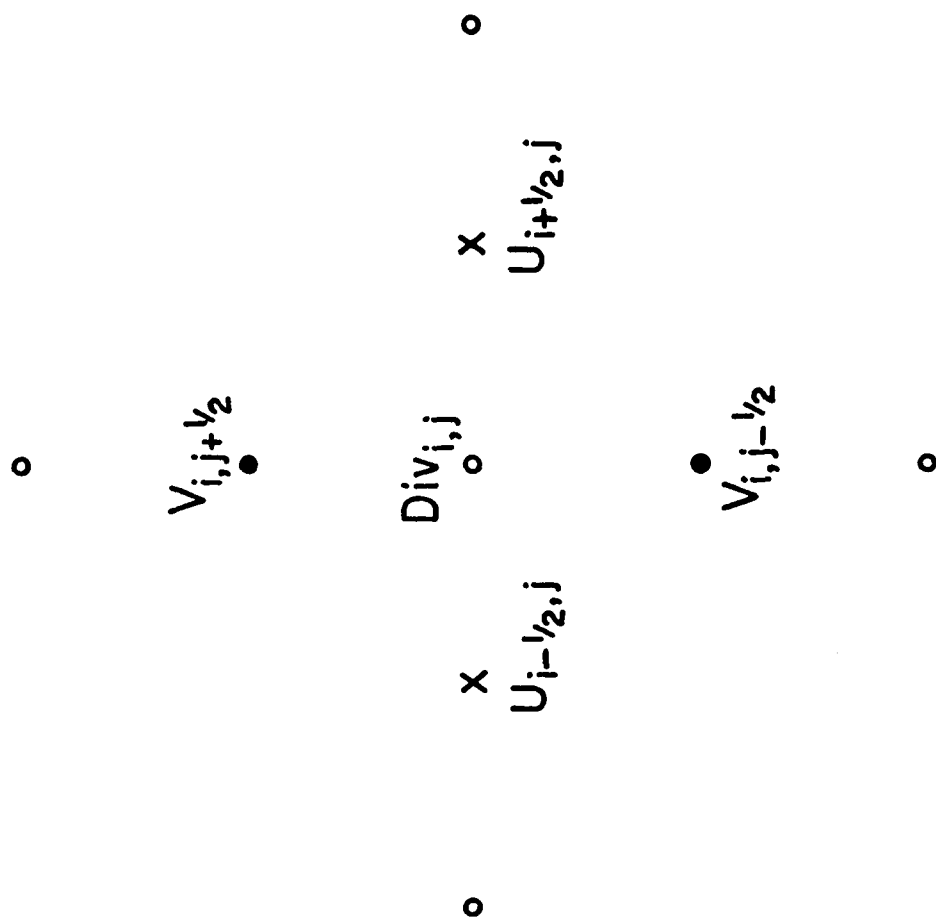


Fig. A.2. Schematic of staggered grid used for finite difference approximation of horizontal derivatives.

This version involves an exponential weighting of the twelve closest data points to perform the analysis. Spatially variable radii of influence are used, and the shape factor of each weight function is proportional to the mean radius. Two passes are conducted with the second pass retaining the same radii used in the first pass. Wavelengths less than two gsu are suppressed.

The data points, or observations, are provided in either a regular, random, or non-random spacing. Smith and Leslie (1984) find that irregular station spacing is an important factor in determining the quality of an objective analysis. With their adaptation of Barnes scheme applied to an analytic function, they discover that irregular station spacing is a significant contributor to short wave variations and to the generation of large perturbations.

From the analyzed u and v fields, the divergence field is calculated. The same finite difference scheme as before is employed. Since it is certain that the divergence field is identically zero, any non-zero values are due to the data interpolation and finite difference approximations. In all cases, this erroneous divergence is assumed to be constant over a 1 km layer, and a corresponding w is calculated from a hydrostatic relationship.

$$w = \frac{-1}{\rho g} \omega \quad (\text{A.4})$$

As a measure of the inaccuracy in w for each case, the root-mean-square (RMS) error is determined as described by Glahn and Lowry (1972).

$$\text{RMSE} = \left[\frac{1}{n} \sum_{j=1}^n (y_j - \hat{y}_j)^2 \right]^{1/2} \quad (\text{A.5})$$

Here, n is the number of grid points, y_j is the actual quantity, and \hat{y}_j is the calculated quantity.

By performing these numerical manipulations on the given stream function, effects of finite differencing and objectively analyzing a data field are demonstrated. Cases are run for six regularly-spaced data meshes. The data spacings range from 2 gsu (225 data points) to 8 gsu (16 data points). Only the 4 gsu data spacing is displayed (case I). Four cases are run using a randomly-spaced data mesh. Each case has a different data point distribution, but each contains 20 points. Two cases are displayed in this work (cases II and III). And, two cases are shown using a data mesh consisting of 20 irregularly-spaced points whose locations are not random (cases IV and V).

The contoured plot of the non-divergent, analytic stream function in Fig. A.1 shows a minimum is present near the center (origin) of the field, and the field is symmetric with respect to a vertical line (y-axis) passing through the origin. If 1 gsu is allowed to equal 100 km, then the units for ψ are m^2/s .

Appearing in Figs. A.3 and A.4 are contoured plots of ψ after the objective analysis scheme is performed. Fig. A.3a uses a regularly-spaced (4 gsu spacing) data mesh consisting of 64 data points. Figs. A.3b and A.3c use randomly-spaced data meshes each made up of 20 points. Figs. A.4a and A.4b employ a non-random mesh which locates 12 data points near the edges of the grid and concentrates 8 data points in the regions of the center and strongest gradient, respectively.

The objective analysis produced from the regularly-spaced data mesh, Fig. A.3a, shows an excellent recreation of the ψ contour pattern. The symmetry is maintained, but the magnitude of the minimum has been reduced by about 6% and the contours have been slightly distorted near the corners. Achtemeier (1986a) has discussed the

impacts of boundaries of a data field upon interpolated values at the grid boundaries.

The objective analysis of the randomly-spaced data points, Figs. A.3b and A.3c, does not produce the high quality result as seen above. Here, the contour patterns display a tilt and have lost their symmetrical structure. For both cases, the magnitude of the minimum has decreased by about 12% to 13%.

The objective analysis of Fig. A.4a is obtained from data points concentrated in the center and nearly restores the magnitude of the cut off minimum. The location of the center has been slightly translated. The region of strong gradient is void of data points, and gradients have been intensified in this region. The analysis done with data points positioned in the region of strongest gradient, Fig. A.4b, exhibits no cut off minimum. Instead a field of wavy contours is produced with a reduction of gradient intensity.

Although not shown, w -fields were constructed for each case. These fields were calculated by using the analyzed u and v fields and by applying a finite difference scheme to approximate the derivatives. Recall that the given stream function is non-divergent so that according to mass continuity, w should be identically zero.

As a measure of error of the ψ and w fields, bar charts of RMS error are shown in Fig. A.5. For a grid spacing of 100 km, the units of RMS error for ψ are m^2/s and for w are cm/s.

Several runs using a regular spaced data set, including case 1, are displayed in Fig. A.5a. As expected, the RMS errors in ψ for a regularly-spaced data mesh increase as the data density decreases. For the randomly-spaced data mesh and the non-randomly-spaced data mesh, the

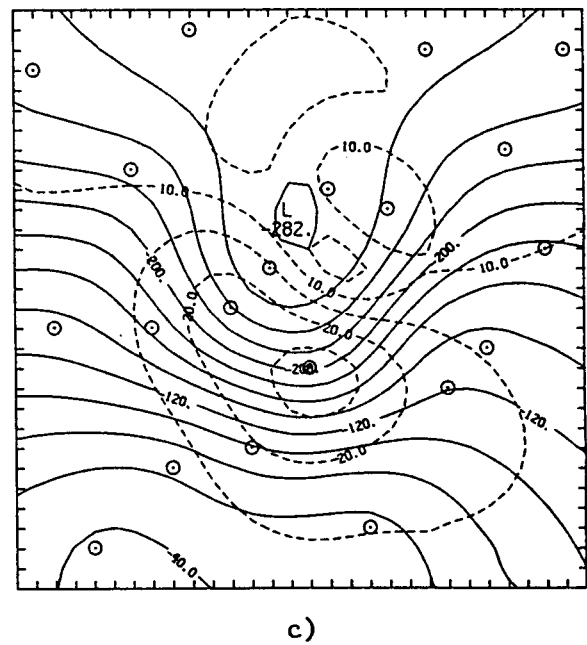
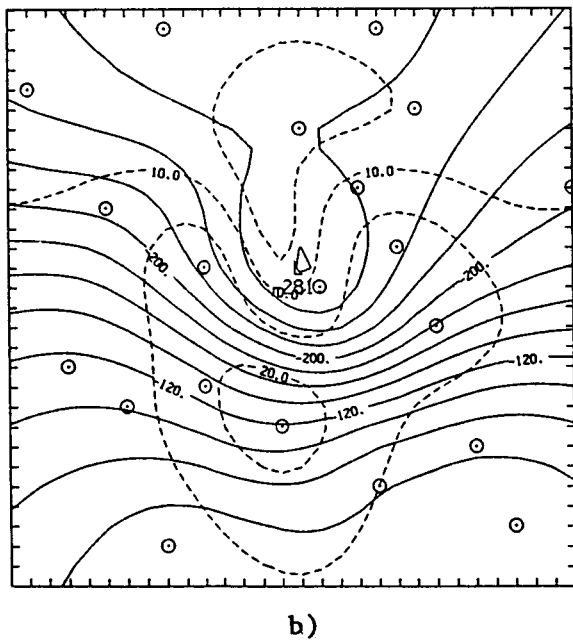
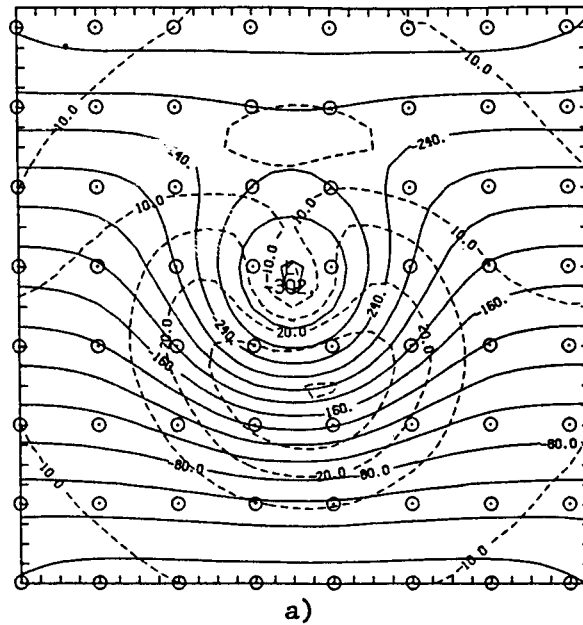
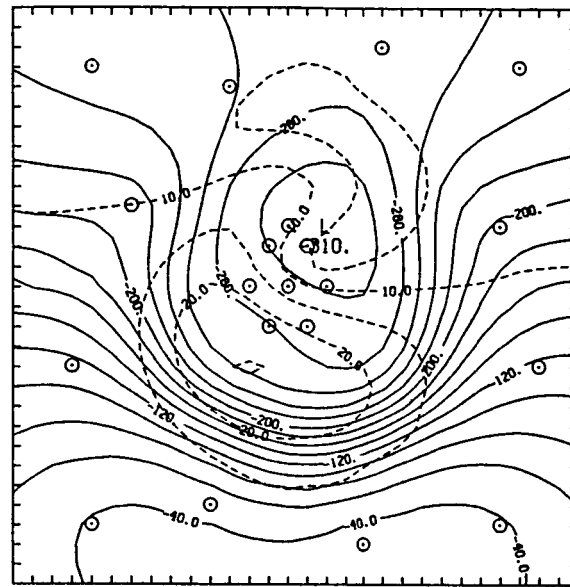
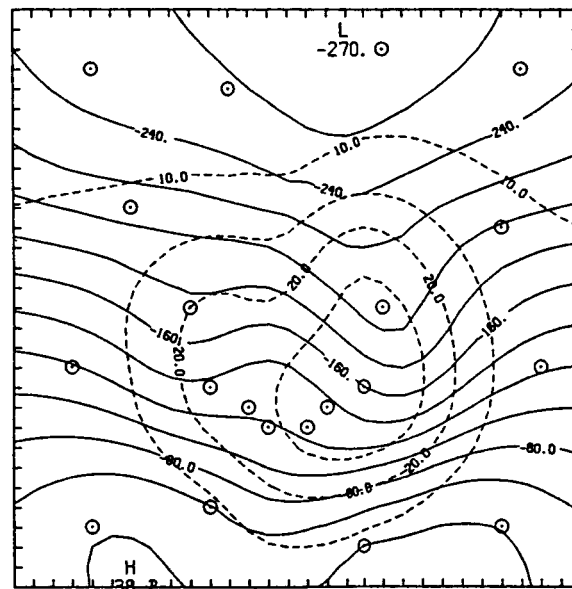


Fig. A.3. Results of the objectively analyzed stream function (solid lines) using a) regularly-spaced data points and b) and c) 20 randomly-spaced data point. Bullseyes indicate locations of data points and dashed lines are isotachs from objectively analyzed horizontal velocities.



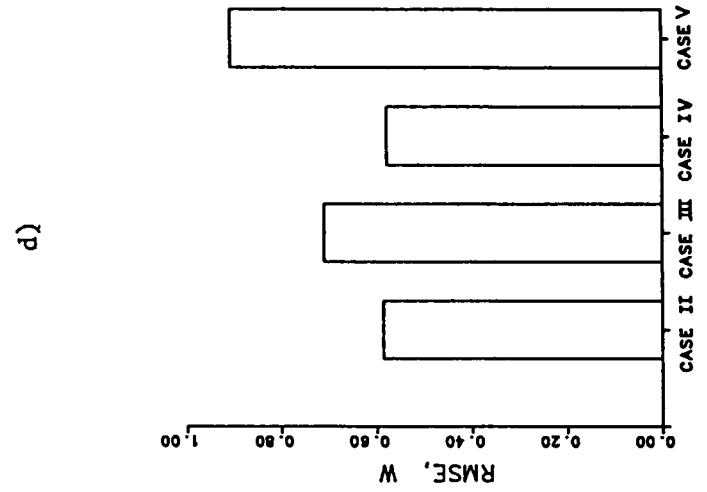
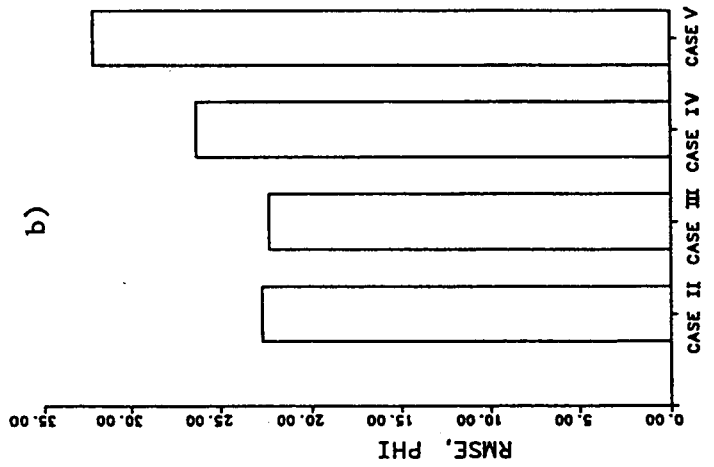
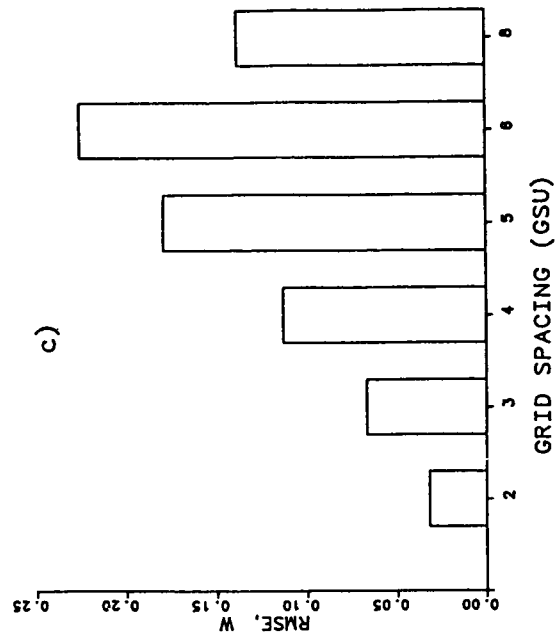
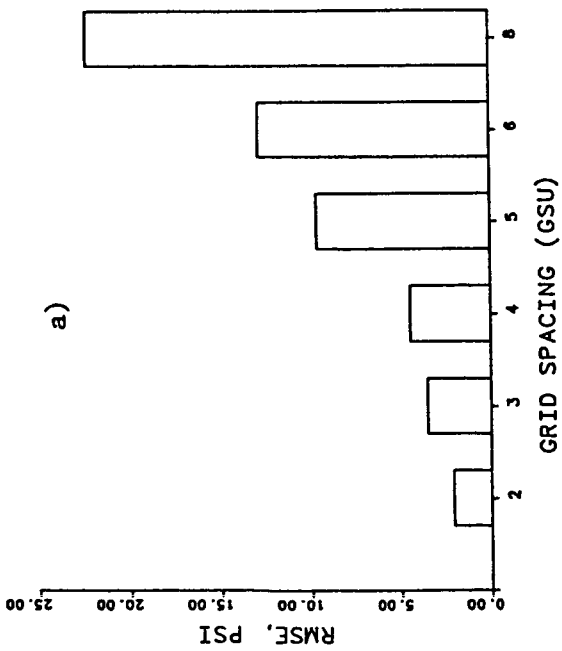
a)



b)

Fig. A.4. Results of objectively analyzed stream function (solid lines) using 20 non-randomly-spaced data points with a concentration of points a) in the minima and b) in the region of strong gradient. Bullseyes and dashed lines as in Fig. A.3:

Fig. A.5. RMS error calculated for a) analyzed ψ fields with regularly-spaced data points (case I is 4 gsu spacing), b) analyzed ψ fields with random (cases II and III) and non-random (cases IV and V) spacings, c) vertical velocity derived from ψ fields of a), and d) vertical velocity derived from ψ fields of b).



RMS errors in ψ appear in Fig. A.5b. These values show that other factors such as data distribution can be significant when performing an objective analysis.

The RMS errors in w for regularly-spaced data meshes and randomly-spaced and non-randomly-spaced data meshes are exhibited in Figs. A.5c and A.5d, respectively. Fig. A.5c shows that the RMS error values increase as the data density decreases, except for the 8 gsu mesh. Here, the data spacing has approached the size of the disturbance. Therefore, the objective analysis scheme only reconstructs the basic state zonal flow which is constant and non-divergent.

In both figures, the RMS errors in w are significant with values up to 0.22 cm/s for a regularly-spaced grid and up to 0.9 cm/s for a randomly-spaced grid. Considering the w -fields for each case, extrema as large as 2 to 3 cm/s are common.

APPENDIX B

ERROR ANALYSIS OF THE ADIABATIC METHOD

An error analysis is performed to determine the mean square error, or error variance, on w calculated from the adiabatic method. Error in this formulation is primarily due to the use of measured quantities in the calculation.

The calculated result, w_c , is separated into two parts: actual, w_A , and error, w_e .

$$w_c = w_A + w_e \quad (B.1)$$

$$= \left[\frac{\partial T / \partial t)_A + v_A \partial T / \partial s)_A}{\Gamma_d - \partial T / \partial h)_A - \partial T_e / \partial h} \right] + \left[\frac{\partial T_e / \partial t + v_A \partial T_e / \partial s + v_e \partial T / \partial s)_A + v_e \partial T_e / \partial s}{\Gamma_d - \partial T / \partial h)_A - \partial T_e / \partial h} \right]$$

where s is the coordinate along a streamline, h is a coordinate in the vertical, and Γ_d is the dry adiabatic lapse rate. By definition of error variance (Neter et al , 1982)

$$\epsilon_{\chi}^2 = \frac{1}{n} \sum \chi^2 \quad (B.2)$$

the form for w is

$$\epsilon_{w_e}^2 = \frac{1}{n} \sum \left[\frac{\partial T_e / \partial t + v_A \partial T_e / \partial s + v_e \partial T / \partial s)_A + v_e \partial T_e / \partial s}{\Gamma_d - \partial T / \partial h)_A - \partial T_e / \partial h} \right]^2 \quad (B.3)$$

This expression is expanded and the sums of cross products, whose terms are assumed to be uncorrelated, are set to 0. This result is

$$\epsilon_{w_e}^2 \approx \frac{1}{n} \sum \left[\frac{\partial T_e / \partial t^2 + v_A^2 \partial T_e / \partial s^2 + v_e^2 \partial T / \partial s)_A^2 + v_e^2 \partial T_e / \partial s^2}{D} \right] \quad (B.4)$$

with

$$(B.5)$$

$$D \approx \Gamma_d^2 - 2\Gamma_d \partial T / \partial h)_A - 2\Gamma_d \partial T_e / \partial h + \partial T / \partial h)_A^2 + 2\partial T / \partial h)_A \partial T_e / \partial h + \partial T_e / \partial h^2$$

If the actual lapse rate is taken to be an average over a layer, then the denominator can be factored outside of the summation

$$\epsilon_{w_e}^2 \approx \frac{1}{nD} \left[\sum \epsilon_{\partial T_e / \partial t}^2 + \sum V_A^2 \epsilon_{\partial T_e / \partial s}^2 + \sum V_e^2 \epsilon_{\partial T / \partial s}^2 + \sum V_e^2 \epsilon_{\partial T_e / \partial s}^2 \right] \quad (B.6)$$

or written in error notation as

$$\epsilon_{w_e}^2 \approx \frac{1}{D} \left[\epsilon_{\partial T_e / \partial t}^2 + \epsilon_{V_A}^2 \epsilon_{\partial T_e / \partial s}^2 + \epsilon_{V_e}^2 \epsilon_{\partial T / \partial s}^2 + \epsilon_{V_e}^2 \epsilon_{\partial T_e / \partial s}^2 \right] \quad (B.7)$$

Now, consider each term individually.

$$\begin{aligned} \epsilon_{\partial T_e / \partial t}^2 &= \frac{1}{n} \sum \left(\frac{T_{e2} - T_{e1}}{\Delta t} \right)^2 = \frac{1}{n \Delta t^2} \sum (T_{e1}^2 + T_{e2}^2 - 2T_{e1}T_{e2}) \\ &= \frac{2}{\Delta t^2} \epsilon_{T_e}^2 \end{aligned} \quad (B.8)$$

Here, the sum of the product of the temperature errors is assumed to be uncorrelated and therefore equal to 0.

$$\epsilon_{V_A}^2 \epsilon_{\partial T_e / \partial s}^2 = \frac{1}{n \Delta s^2} \sum V_A^2 (T_{e1}^2 + T_{e2}^2 - 2T_{e1}T_{e2}) = \frac{2}{\Delta s^2} \overline{V_A^2} \epsilon_{T_e}^2 \quad (B.9)$$

Again, the sum of the product of temperature errors is uncorrelated with the added assumption that the mean squared velocity is representative of a layer.

$$\epsilon_{V_e}^2 \epsilon_{\partial T / \partial s}^2 \approx \epsilon_{V_e}^2 \epsilon_{\partial T_e / \partial s}^2 \quad (B.10)$$

This assumption is fashioned after Godman's (1962) results with the additional premise that the mean value of these quantities is 0. The variance in the temperature gradient is found using all reporting

stations at all time periods and employing the following formula,

$$\epsilon_{\partial T / \partial s}^2 = \frac{1}{n} \sum_i^n (\partial T / \partial s_i - \overline{\partial T / \partial s})^2 \quad (\text{B.11})$$

where the subscript i indicates a given station location.

The final term is

$$\begin{aligned} \epsilon_{V_e \partial T_e / \partial s}^2 &\approx \epsilon_{V_e}^2 \epsilon_{\partial T_e / \partial s}^2 \approx \epsilon_{V_e}^2 \frac{1}{n \Delta s} \sum (T_{e1}^2 + T_{e2}^2 - 2T_{e1}T_{e2}) \\ &\approx \epsilon_{V_e}^2 \frac{2}{\Delta s} \epsilon_{T_e}^2 \end{aligned} \quad (\text{B.12})$$

Here, Godman's result is used along with the assumption that the sum of the product of temperature errors is 0.

<u>P(mb)</u>	<u>RMSE_T (K)</u>
100	2.0
200	3.0
300	3.0
400	2.6
500	2.0
600	1.5
700	1.5
800	1.5
900	1.5
1000	1.5

Table B.1. Root mean square error (RMSE) of observed temperatures.

The error values for wind and temperature measurements with height are listed in Table B.1. A value of 1K is cited by (Air Weather Service, 1955) as a suitable estimate of temperature measurement error of rawinsondes.

LIST OF REFERENCES

- Achtemeier, G. L., 1975: On the Initialization Problem: A Variational Adjustment Method., Mon. Wea. Rev., 103, 1089-1103.
- Achtemeier, G. L., H. T. Ochs, and S. Q. Kidder, 1984: A Diagnostic Numerical Model for the Application of Satellite Data for the Study of Global Weather Systems. Preprints, First Conference on Satellite Meteorology/Remote Sensing and Applications, Clearwater, FL, 260.
- Achtemeier, G. L., 1986a: The Impact of Data Boundaries upon a Successive Corrections Objective Analysis of Limited-Area Datasets., Mon. Wea. Rev., 114, 40-49.
- Achtemeier, G. L., H. T. Ochs, S. Q. Kidder, and R. W. Scott, 1986b: Evaluation of a Multivariate Variational Assimilation of Conventional and Satellite Data for the Diagnosis of Cyclone Systems. Preprints, Second Conference on Satellite Meteorology/Remote Sensing and Applications, Williamsburg, VA, 76-81.
- Achtemeier, G. L., H. T. Ochs, S. Q. Kidder, R. W. Scott, J. Chen, D. Isard, and B. Chance, 1986c: A Variational Assimilation Method for Satellite and Conventional Data: Development of Basic Model for Diagnosis of Cyclone Systems. NASA Contractor Report, NAS8-34902, Marshall Space Flight Center, 223 pp.
- Achtemeier, G. L., H. T. Ochs, S. Q. Kidder, and R. W. Scott, 1985: Evaluation of a Multivariate Variational Assimilation of Conventional and Satellite Data for the Diagnosis of Cyclone Systems. Preprints, International Symposium on Variational Methods in Geosciences, Norman, OK, (in press).

- Air Weather Service, 1955: Accuracies of Radiosonde Data, United States Air Force Technical Report 105-133, 12 pp.
- Alberty, R. L., D. W. Burgess, and T. T. Fujita, 1980: Severe Weather Events of 10 April 1979. Bull. Amer. Meteor. Soc., 62, 1577-1590.
- Barnes, S. L., 1973: Mesoscale Objective Map Analysis Using Weighted Time-Series Observations. NOAA Technical Memorandum, ERL NSSL-62, 60 pp.
- Belt, C. L. and H. E. Fuelberg, 1982: The Effects of Random Errors in Rawinsonde Data on Derived Kinematic Quantities. Mon. Wea. Rev., 110, 91-101.
- Carlson, T. N., R. A. Anthes, M. Schwartz, S. G. Benjamin, and D. G. Baldwin, 1980: Analysis and Prediction of Severe Storms Environment. Bull. Amer. Meteor. Soc., 61, 1018-1032.
- Chien, H. and P. J. Smith, 1973: On the Estimation of Kinematic Parameter in the Atmosphere from Radiosonde Wind Data. Mon. Wea. Rev., 101, 252-261.
- Djuric, D., 1969: Note on Estimation of Vertical Motion by the Omega Equation. Mon. Wea. Rev., 97, 902-904.
- Fankhauser, J. C., 1969: Convective Processes Resolved by Mesoscale Rawinsonde Network. J. Appl. Meteor., 8, 778-798.
- Forsyth, G. E. and W. R. Wasow, 1960: Finite-Difference Methods for Partial Differential Equations. J. Wiley and Sons, Inc., New York, 444 pp.
- Fuelberg, H. E. and W. S. Lee, 1985: A Comparison of Adiabatic and Kinematic Vertical Motions Using Mesoscale Data. Preprints, Fourteenth Conference on Severe Local Storms, Indianapolis, IN,

417-423.

Gibson, J., 1984: GOES Data Users' Guide, National Environmental Satellite, Data, and Information Service, Washington D.C.

Glahn, H. R. and D. A. Lowry, 1972: The Use of Model Output Statistics (MOS) in Objective Weather Forecasting. J. Appl. Meteor., 11, 1203-1211.

Godman, L. A., 1962: The Variance of the Product of K Random Variables. J. Amer. Stat. Assoc., 57, 54-60.

Griffin, C. G., W. L. Woodley, P. G. Grube, D. W. Martin, J. Stout, and D. N. Sikdar, 1978: Rain Estimation from Geosynchronous Satellite Imagery-Visible and Infrared Studies. Mon. Wea. Rev., 106, 1153-1171.

Holton, J. R., 1979: An Introduction to Dynamic Meteorology, second edition. Academic Press, New York, 391 pp.

Homan, J. H. and D. G. Vincent, 1983: Mesoanalysis of Surface Variables During the Severe Storm Outbreak of 10-11 April 1979. Mon. Wea. Rev., 111, 1122-1130.

Kung, E. C., 1972: A Scheme for Kinematic Estimate of Large-Scale Vertical Motion with an Upper Air Network. Quart. J. Roy. Meteor. Soc., 98, 402-411.

Kung, E. C., 1973: Note on Design of an Optimized Computation Scheme for Kinematic Vertical Motion Fields. Mon. Wea. Rev., 101, 685-690.

Kurihara, Y., 1961: Accuracy of Winds aloft Data and Estimation of Error in Numerical Analysis of Atmospheric Motions. J. Meteor. Soc. Japan, 39, 331-45.

Lamb, P. J. and D. H. Portis, 1986: On the Estimation of Vertical

Motion for the Diagnosis of Summer Rainfall Fluctuations in the Central United States. Proceedings, First WMO Workshop on the Diagnosis and Prediction of Monthly and Seasonal Atmospheric Variations over the Globe, Geneva, (in press).

Lateef, M. A., 1967: Vertical Motion, Divergence and Vorticity in the Troposphere over the Caribbean, August 3-5, 1963. Mon. Wea. Rev., 95, 778-790.

Miller A. and H. A. Panofsky, 1958: Large-Scale Vertical Motion and Weather in January, 1953. Bull. Amer. Meteor. Soc., 39, 8-13.

Moore, J. T. and H. E. Fuelberg, 1981: A Synoptic Analysis of the First AVE-SESAME '79 Period. Bull. Amer. Meteor. Soc., 62, 1577-1590.

Neter, J., W. Wasserman, and G. A. Whitmore, 1982: Applied Statics, second edition. Allyn and Bacon, Inc., Boston, 773 pp.

O'Brien, J. J., 1970: Alternative Solutions to the Classical Vertical Velocity Problem. J. Appl. Meteor., 9, 197-203.

O'Neill, T. H. R., 1966: Vertical Motion and Precipitation Computations. J. Appl. Meteor., 5, 595-605.

Oppenheim, A. V. and R. W. Schaffer, 1975: Digital Signal Processing. Prentice-Hall, Englewood Cliff, New Jersey, 585 pp.

Panofsky, H. A., 1946: Methods of Computing Vertical Motions in the Atmosphere. J. Meteor., 3, 45-49.

Panofsky, H. A., 1964: Introduction to Dynamic Meteorology, first edition. The Pennsylvania State University, University Park, Pennsylvania, 243 pp.

Pedder, M. A., 1981: On the Errors of Kinematic Vertical Motion Estimation Using Divergence Bias Adjustment Procedures. Mon. Wea.

Rev., 109, 1813-1816.

Pettersen, S., 1956: Weather Analysis and Forecasting, Vol. 1, second edition, McGraw-Hill Book Co., Inc., New York, 428 pp.

Phillips, N. A., 1957: A Coordinate System having some Special Advantages for Numerical Forecasting. J. Meteor., 14, 184-186.

Sasaki, Y., 1958: An Objective Analysis Based on the Variational Method. J. Meteor. Soc. Japan, 36, 77-88.

Shuman, F. G. and J. B. Hovermale, 1968: An Operational Six-Layer Primitive Equation Model. J. Appl. Meteor., 7, 525-547.

Smith, D. R. and F. W. Leslie, 1984: Error Determination of a Successive Correction Type Objective Analysis Scheme. J. Atmos. Ocean. Tech., 1, 120-130.

Smith, P. J., 1971: An Analysis of Kinematic Vertical Motions. Mon. Wea. Rev., 99, 715-724.

Smith, P. J., and C. P. Lin, 1978: A Comparison of Synoptic Scale Vertical Motions Computed by the Kinematic Method and Two Forms of the Omega Equation. Mon. Wea. Rev., 106, 1687-1694.

Stuart, D. W., 1974: A Comparison of Quasi-Geostrophic Vertical Motion Using Various Analyses. Mon. Wea. Rev., 102, 363-374.

Vincent, D. G. and J. H. Homan, 1983: Mesoscale Analysis of Pressure and Precipitation Patterns During AVE-SESAME 1979, 10-11 April. Bull. Amer. Meteor. Soc., 64, 23-28.

White, G. H., 1983: Estimates of Seasonal Mean Vertical Velocity Fields of the Extratropical Northern Hemisphere. Mon. Wea. Rev., 111, 1418-1431.

1. REPORT NO. NASA CR-4022		2. GOVERNMENT ACCESSION NO.		3. RECIPIENT'S CATALOG NO.	
4. TITLE AND SUBTITLE Application of Satellite Data to the Variational Analysis of the Three Dimensional Wind Field				5. REPORT DATE October 1986	
				6. PERFORMING ORGANIZATION CODE	
7. AUTHOR(S) Barbara Ann Chance				8. PERFORMING ORGANIZATION REPORT #	
9. PERFORMING ORGANIZATION NAME AND ADDRESS University of Illinois Urbana-Champaign, Illinois 61820				10. WORK UNIT NO. M-539	
				11. CONTRACT OR GRANT NO. NAS8-35530	
				13. TYPE OF REPORT & PERIOD COVERED Contractor Report	
12. SPONSORING AGENCY NAME AND ADDRESS National Aeronautics and Space Administration Washington, D.C. 20546				14. SPONSORING AGENCY CODE	
15. SUPPLEMENTARY NOTES Contract Monitor: John Kaufman, Atmospheric Sciences Division, Systems Dynamics Laboratory, Marshall Space Flight Center, Alabama 35812					
16. ABSTRACT <p>A vertical velocity algorithm is developed which blends the strengths of two commonly used techniques, the O'Brien corrected kinematic method and the adiabatic method. These two constituent methods are based on different principles. The kinematic method is based on mass continuity, and the adiabatic method is based on the First Law of Thermodynamics. By blending the methods using numerical variational analysis, a final vertical motion estimate is obtained possessing information from diverse atmospheric processes.</p> <p>To assign the contribution of each method, a weighting function is constructed. The function weights between O'Brien corrected kinematic divergence values and the adiabatic estimate of vertical motion. Criteria are determined so that more influence is accorded to that estimate which better agrees with physical processes.</p> <p>This algorithm is tested with the AVE-SESAME I data set. The results show that the variational result in most cases succeeded in finding a compromise between the two techniques. A triumph of the algorithm is providing reasonable magnitudes of vertical velocity in the lower stratosphere.</p> <p>Problems with the variational algorithm are of both meteorological and numerical nature. A finer resolution data set may reduce the meteorological difficulties. A different approach to the final solution could resolve the numerical problem, even though the solution employed in this work is theoretically correct.</p>					
17. KEY WORDS Satellite Weather Variational Analysis Kinematic Method Remote Wind Sensing Global Atmospheric Circulation			18. DISTRIBUTION STATEMENT Unclassified - Unlimited Subject Category 47		
19. SECURITY CLASSIF. (of this report) Unclassified		20. SECURITY CLASSIF. (of this page) Unclassified		21. NO. OF PAGES 93	
				22. PRICE A05	